Paleointensity of the ancient Martian magnetic field

Benjamin P. Weiss,[1] Luis E. Fong,[2] Hojatollah Vali,[3,4] Eduardo A. Lima,[1] and Franz J. Baudenbacher[2,5]

Received 13 August 2008; revised 26 October 2008; accepted 30 October 2008; published 13 December 2008.

[1] Mars today has no core dynamo magnetic field. However, the discovery of remanent magnetization in Martian meteorites and intense crustal magnetization suggests that Mars once had a global field. Here we present high resolution maps of the magnetic field of Martian meteorite ALH 84001. These maps are the most sensitive yet quantitative study of natural remanent magnetization (with resolved anomalies as weak as 1×10^{-14} Am^2). ALH 84001 likely contains a 4 billion year old (Ga) thermoremanence partially overprinted by one or more poorly understood secondary components. Our data suggest that the paleointensity of the local paleofield was within an order of magnitude of that of the present-day Earth. If this field were global in extent, it should have played a key role in Martian atmospheric and climatic evolution. However, it is still too weak to easily explain the intensity of Martian crustal paleomagnetic anomalies. **Citation:** Weiss, B. P., L. E. Fong, H. Vali, E. A. Lima, and F. J. Baudenbacher (2008), Paleointensity of the ancient Martian magnetic field, *Geophys. Res. Lett.*, *35*, L23207, doi:10.1029/2008GL035585.

1. Introduction

[2] The intensities of surface magnetic fields on Mars during most of the planet's history are essentially unknown. Magnetic anomalies reside primarily in crustal terranes >3.8 billion years old (Ga) and are weak or absent within younger impact basins. These data have been used to argue that an early field had decayed by ~3.9 Ga [*Acuna et al.*, 1999], but the low spatial resolution of spacecraft field data combined with the lack of precise ages for the crustal sources make this timing highly uncertain. Understanding the history of Martian fields is critical for understanding the planet's thermal, tectonic, and climatic evolution.

[3] Of the nearly 50 known Martian meteorites, only a single sample—the meteorite ALH 84001—dates back to the early field epoch. ALH 84001 indeed contains a natural remanent magnetization (NRM). The NRM resides mainly in single domain stoichiometric magnetite- and pyrrhotite-bearing carbonate [*Antretter et al.*, 2003; *Rochette et al.*, 2005; *Weiss et al.*, 2002a; *Weiss et al.*, 2004], as well as possibly carbonate-associated hematite [*Steele et al.*, 2007] and free magnetite [*Steele et al.*, 2007], sulfides [*Kirschvink et al.*, 1997] and chromite [*Weiss et al.*, 2002a]. All paleomagnetic studies of ALH 84001 have found that the NRM is heterogeneously oriented at fine scales [*Antretter and Fuller*, 2002; *Antretter et al.*, 2003; *Collinson*, 1997; *Kirschvink et al.*, 1997; *Weiss et al.*, 2000; *Weiss et al.*, 2002b]. Bulk (tens of mg and larger) samples do not show significant remanence or susceptibility anisotropy [*Collinson*, 1997; *Gattacceca et al.*, 2005; *Weiss et al.*, 2000].

[4] ^{40}Ar/^{39}Ar data suggest that the characteristic NRM in ALH 84001, which has been observed as an origin-trending component blocked above coercivities of ~40 mT [*Antretter et al.*, 2003; *Gattacceca and Rochette*, 2004], was likely acquired as a thermoremanence on Mars during a shock event that strongly heated the meteorite at ~4 Ga [*Shuster and Weiss*, 2005; *Weiss et al.*, 2002a]. Noble gas geochronology and a variety of geochemical and petrographic data collectively indicate that the meteorite has not been heated to temperatures above ~500°C since this time. The heterogeneous pattern of magnetization and evidence for one or more shock events following carbonate formation suggest that it likely later acquired secondary overprints (see auxiliary material).[1] The characteristic NRM could have been the product of either a dynamo or local crustal paleofield. However, given that any strong crustal paleofields would likely have been the product of an earlier dynamo, this suggests that a dynamo existed on Mars at or before 3.9 Ga.

[5] Although the age of the characteristic NRM in ALH 84001 is reasonably well known, the intensity of the paleofield that magnetized it is not. Previous experiments on the meteorite using the ratio of the NRM to saturation isothermal remanent magnetization (sIRM) method have obtained paleointensity values ranging from several to several tens of microteslas (μT) (for comparison, the Earth's surface field today has an intensity of ~50 μT), with a striking dependence on the mass of the sample used for the analysis (Figure S1). Although the NRM/sIRM method should only yield an order-of-magnitude estimate of the paleointensity even for single-component NRM (see auxiliary material) [*Weiss et al.*, 2007a], a key reason for this large range of values must also be the nonunidirectional orientation of the fine scale magnetization in ALH 84001 [*Weiss et al.*, 2000; *Weiss et al.*, 2002b], which would mean that measurements of bulk grains provide only a lower limit on the true paleointensity. It is therefore possible that the Martian paleofield at 4 Ga was in fact significantly stronger than that of the Earth today. A strong field would then make it

[1]Department of Earth, Atmospheric, and Planetary Sciences, Massachusetts Institute of Technology, Cambridge, Massachusetts, USA.
[2]Department of Physics and Astronomy, Vanderbilt University, Nashville, Tennessee, USA.
[3]Department of Anatomy and Cell Biology and Facility for Electron Microscopy Research, McGill University, Montreal, Quebec, Canada.
[4]Department of Earth and Planetary Sciences, McGill University, Montreal, Quebec, Canada.
[5]Department of Biomedical Engineering, Vanderbilt University, Nashville, Tennessee, USA.

0094-8276/08/2008GL035585$05.00

[1]Auxiliary materials are available in the HTML. doi:10.1029/2008GL035585.

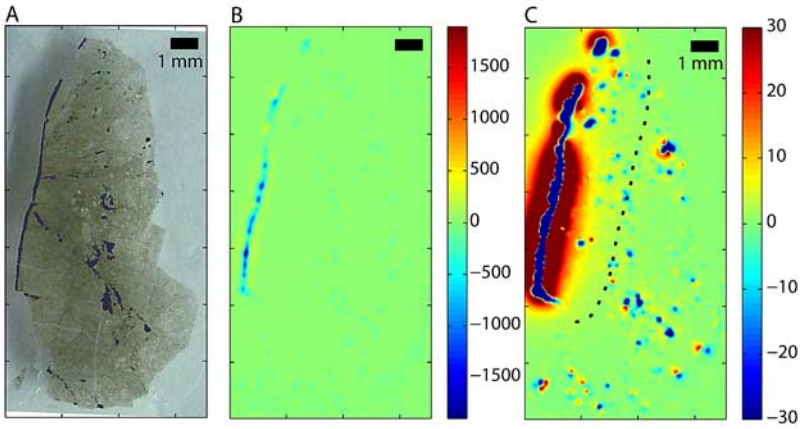

Figure 1. Natural remanent magnetization (NRM) field of ALH 84001. (a) Reflected light photograph of 30 μm thin section 227b,2 showing pyroxene (light brown), fusion crust along left side (black) and chromite (black interior grains). (b) Vertical component of the NRM field as measured 140 μm above the sample. Positive (out-of-the-page) fields are red and yellow and negative (into-the-page) fields are blue. The field is dominated by the fusion crust. (c) Same as Figure 1b except with color scale stretched to show weak magnetism of meteorite interior. Approximate boundary of baked zone is shown by dashed line.

much easier to explain the intensity of the Martian crustal anomalies, which are ten times as intense as those in the Earth's continental crust [*Connerney et al.*, 1999].

[6] At the outset of this study, we hypothesized that this mass dependence of paleointensity estimates is not accidental but is rather causal. If so, then there are at least two possible reasons why small samples would give higher paleointensities: (a) the smaller samples have larger magnetic anisotropy which could result in an overestimate of their paleointensities [*Selkin et al.*, 2000] (and possibly also explain the nonunidirectional NRM [*Antretter et al.*, 2003]), or (b) the small samples are magnetically isotropic and the net NRM of large samples underestimates the true fine-scale thermoremanent NRM and therefore the true paleointensity.

[7] To distinguish between hypotheses (a) and (b), we used the low-transition temperature Superconducting Quantum Interference Device Microscope (SM) [*Fong et al.*, 2005; *Weiss et al.*, 2007a, 2007b] to resolve the fine-scale heterogeneity of the magnetization and obtain more accurate paleointensity estimates from resolved anomalies. The masses of these anomalies are only several hundred nanograms and they contain millions of ferromagnetic crystallites. These maps afford us the opportunity to study the paleomagnetism of samples with effective masses $\sim$10,000 times less than that of the next largest samples previously analyzed.

2. Methods

[8] All of the magnetic data presented here were acquired using the SQUID Microscope, a low-transition temperature magnetometer that maps the vertical component of the magnetic fields of room temperature samples [*Weiss et al.*, 2007b]. The SM was equipped with a monolithic DC SQUID sensor with an effective diameter of 80 μm and was rastered over the sample at a constant height of 140 μm to map the field at a rectangular grid of thousands of locations spaced by 40 μm. All data were acquired inside a two-layer mu-metal shielded room (DC field <50 nT and AC field peak-to-peak variations <0.05 nT at 0.01 Hz). In this configuration, the SM can resolve individual dipoles with a moment resolution of $\sim 10^{-15}$ Am^2 and a spatial resolution of $\sim$140 μm. Unlike standard SQUID moment magnetometers, the SM does not measure the sample's bulk moment but rather maps its magnetic field in order to resolve magnetization variation within the sample. This requires that the sample magnetization be constrained from least squares fits to the field data.

[9] We used the SM to map ALH 84001,227b,2, a 30 μm thin section taken from directly underneath thin section 227b,1 that we previously studied using a lower resolution (250 μm) SM [*Weiss et al.*, 2002b]. The thin section represents a partial cross section of the parent meteorite (Figure 1), beginning with a semi-continuous rim of fusion crust at left produced during passage through the Earth's atmosphere and proceeding to the meteorite's interior unaffected by atmospheric heating at right.

[10] Using the SM, we imaged the evolution of the NRM during progressive three-axis AF demagnetization from 5 to 100 mT in steps of 5 or 10 mT. We also measured stepwise IRM acquisition in the out-of-the-thin-section-plane direction (IRM$_z$) from 20 to 545 mT, as well as IRM 545 mT in the two in-plane directions (IRM$_x$ and IRM$_y$) (see auxiliary material). Following the magnetic analyses, we imaged the sample using optical and electron microscopy at McGill University (see auxiliary material).

3. Measurements

[11] SM measurements of the NRM revealed three main zones of magnetization associated with the fusion crust, an adjacent baked zone, and the meteorite interior (Figure 1). An intense, relatively uniform field oriented into the plane of the thin section is present above the fusion crust at left and extends $\sim$0.1 mm into the interior, surrounded by a belt of oppositely oriented ("return flow") field. Above the meteorite's deep interior at right are much weaker fields with higher spatial frequencies and multiple zero-crossings. Located between the fusion crust and deep interior zones and extending $\sim$2 mm into the meteorite is a region

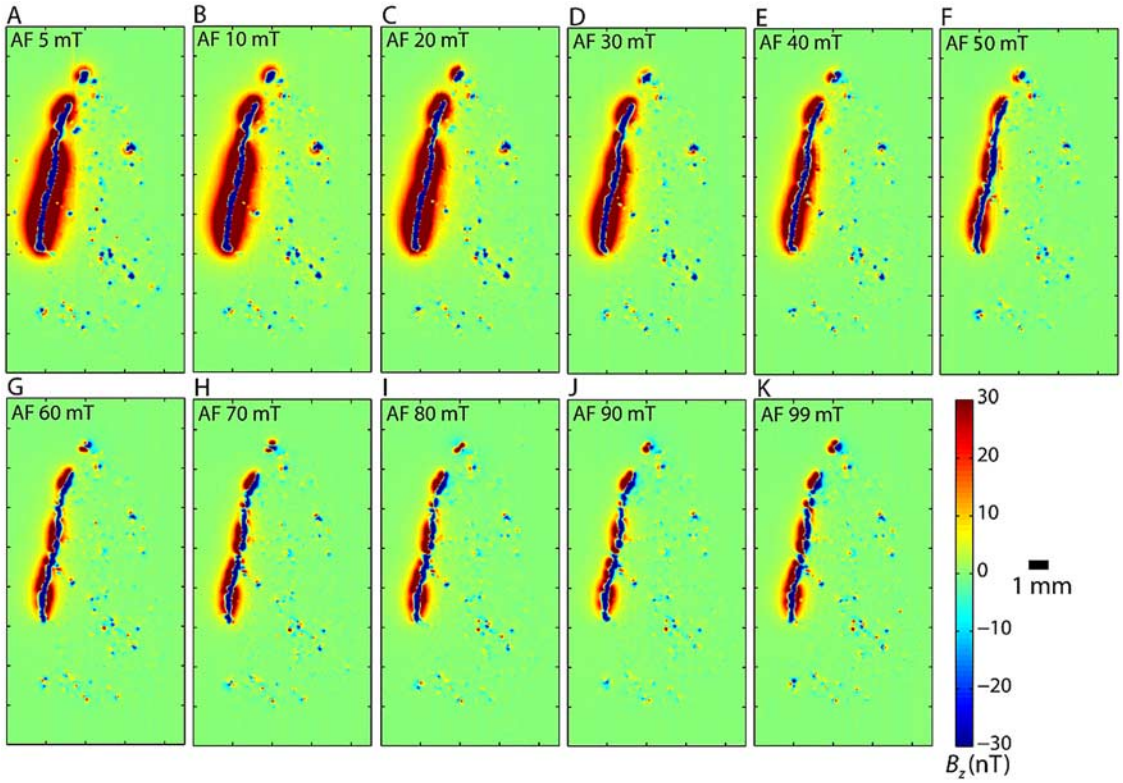

Figure 2. Evolution of natural remanent magnetization field of ALH 84001 during progressive three axis alternating field (AF) demagnetization. Shown is the vertical component of the field as measured 140 μm above the sample; positive (out-of-the-page) fields are red and yellow and negative (into-the-page) fields are blue. All images share 1 mm scale bar and intensity scale at lower right. (a) After a peak AF of 5 mT. (b) AF 10 mT. (c) AF 20 mT. (d) AF 30 mT. (e) AF 40 mT. (f) AF 50 mT. (g) AF 60 mT. (h) AF 70 mT. (i) AF 80 mT. (j) AF 90 mT. (k) AF 99 mT.

exhibiting intermediate behavior: like the deep interior, it is unmelted and has weak magnetic anomalies associated with carbonate and chromite, but like the fusion crust, individual anomalies are concentrically zoned with interior downward fields ringed by belts of upward fields.

[12] Fields above the interior are often spatially correlated with carbonate and chromite grains. Our electron microscopy and IRM data (see auxiliary material) indicate that pyrrhotite and magnetite intimately associated with the nonmagnetic macroscopic carbonate and chromite are the actual sources of this magnetization. In particular, high-resolution transmission electron microscopy analysis of an ultrathin section prepared by focused ion beam milling from an individual grain of chromite (Figure S3) detected enclosed sulfide containing lattice fringes with $\underline{d}$-spacings indicative of monoclinic pyrrhotite (see auxiliary material).

[13] We conducted separate unidirectional least squares fits to both the full NRM scan as well as to the interior-only (no fusion crust) portion (see auxiliary material). From both inversions (data not shown), we obtained residuals that far exceeded our measurement noise, confirming that the meteorite is not unidirectionally magnetized. To characterize the NRM pattern in more detail, we then selected 41 relatively isolated anomalies (Figure S4) and conducted unidirectional least squares fits to solve for each anomaly's magnetization intensity and direction. NRM intensities from individual anomalies range from 4×10^{-14} Am^2 (deep interior anomaly 41) to 6×10^{-10} Am^2 (fusion crust anomaly 14). As expected, the fit NRM directions are widely scattered (Figure S9a).

[14] The two fusion crust anomalies (3 and 14) collectively carry the majority of the magnetization in the sample. A uniformity test [*Watson*, 1956] demonstrates that the remaining 39 anomalies are nonrandomly distributed to >99% confidence and are preferentially oriented in the direction of the fusion crust. However, when the 16 anomalies from the fusion crust and intermediate zone (within 3 mm of the fusion crust), which are mainly magnetized downward like the fusion crust, are excluded from the population, randomness *cannot* be rejected with 99% confidence (Figure S9a). This result serves as a joint conglomerate and baked contact test, demonstrating that the deep interior of the meteorite has a preterrestrial NRM that survived atmospheric passage, sample handling by NASA, and the production of the thin section. By analogy with our previous SM studies of ALH 84001, the fusion crust magnetization is a thermoremanence acquired during atmospheric passage in the Earth's field. Its great intensity relative to the interior is mainly due to the relatively high concentration of cryptocrystalline magnetite that forms in the fusion crusts of stony meteorites [*Genge and Grady*, 1999]. Previous studies have shown that thermal remagnetization from atmospheric passage extends from 0.1 to several mm into the unmelted interiors of stony meteorites [*Butler*, 1972; *Sugiura and Strangway*, 1983; *Weiss et al.*, 2000; *Weiss et al.*, 2002b].

[15] The sample field as imaged during progressive AF demagnetization (Figure 2) was broadly similar to the

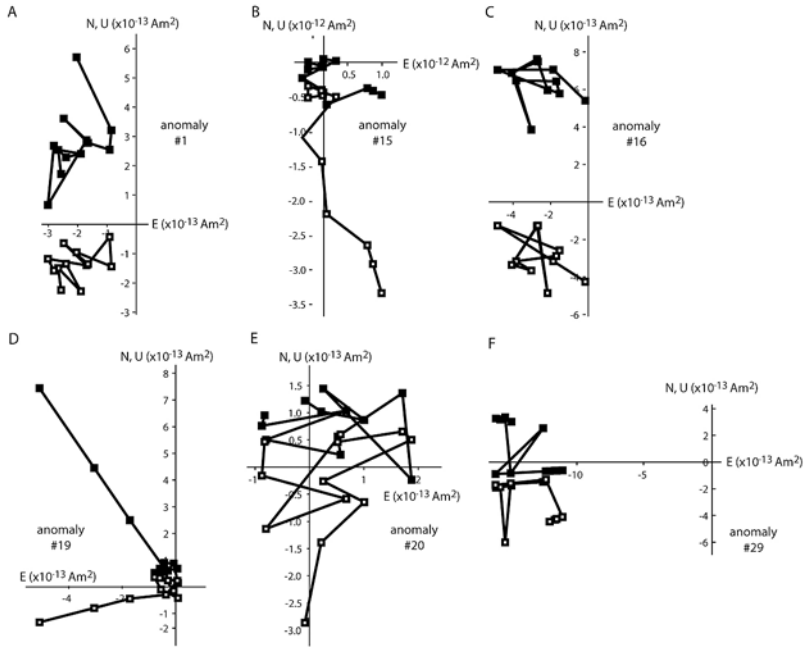

Figure 3. Evolution of natural remanent magnetization (NRM) during alternating field (AF) demagnetization of selected anomalies as inferred from least squares inversion of SQUID Microscope maps of ALH 84001 (Figures 1 and 2). Closed (open) symbols represent end points of magnetization projected onto horizontal (vertical) planes. Shown for each anomaly is the NRM and moment after AF demagnetization to 5 mT, 10 mT, 20 mT, 30 mT, 40 mT, 50 mT, 60 mT, 70 mT, 80 mT, 90 mT, and 99 mT. (a) Anomaly 1. (b) Anomaly 15. (c) Anomaly 16. (d) Anomaly 19. (e) Anomaly 20. (f) Anomaly 29. The scatter in moments visible at high AF steps (e.g., anomaly 20 at AF > 20 mT) is due to a combination of spurious remanence induced by our AF system and uncertainties in the magnetization fit due to surrounding magnetization.

NRM, with intense, downward fields above the fusion crust and weaker, heterogeneously oriented fields above carbonates and chromite in the interior. As AF demagnetization progressed to higher peak fields, the intensity of the fields decreased and the magnetization weakened. Again, our inversions (Figure 3) show that the meteorite cannot be unidirectionally magnetized even after AF demagnetization to 5–30 mT (Figures S9b–S9e). By AF 40 mT (Figure S9f–S9l), many anomalies (including essentially all those dominated by magnetite; see Figures 3d and 3e) have been significantly demagnetized and are either too weak to yield high fidelity inversions or else have directions dominated by spurious remanence induced by our AF system. Weak NRM after AF 99 mT remained in anomalies dominated by pyrrhotite, as expected for this high-coercivity mineral. Such high stability has also been observed from studies of bulk ALH 84001 grains [*Antretter et al.*, 2003; *Collinson*, 1997; *Gattacceca and Rochette*, 2004; *Kirschvink et al.*, 1997]. By AF 99 mT, the intensity of anomaly 41 had dropped to 1.2×10^{-14} Am^2. This is by nearly two orders of magnitude the weakest measured NRM in the history of paleomagnetism.

[16] Using these data, we calculated 41 individual NRM/sIRM paleointensities for the thin section. The fusion crust and baked zone have Earth-strength paleointensities, giving a median value of 34 μT. This is as expected given that the magnetization in these zones was acquired at 13 ka during landing on Earth [*Jull et al.*, 1995]. The interior anomalies have a median paleointensity of 46 μT, with 95% of the anomalies having a paleointensity within a factor 6 of the median (Figure S10). As observed for a SM paleointensity study of terrestrial basalt [*Weiss et al.*, 2007a], there is a sparsely populated high-field tail to the paleointensity distribution which may be a reflection of the expected variability of grain sizes and volumes amongst the anomalies. Our SQUID microscopy study of anisotropy of IRM (see auxiliary material) found no evidence that the anomalies have strong magnetic anisotropy that might bias these paleointensity estimates or be responsible for the heterogeneous orientation of their NRM directions. Assuming that the heterogeneous magnetization in the meteorite is the product of early shock events (see auxiliary material), these data would suggest that a field of order Earth-strength magnetized the interior of ALH 84001 at 4 Ga.

4. Conclusions

[17] Our new paleointensity estimate matches those derived from the smallest previously studied samples [*Gattacceca and Rochette*, 2004; *Kirschvink et al.*, 1997]. This indicates that our study has captured (indeed, well exceeded) the smallest characteristic spatial scale of the NRM and that our paleointensity estimates are not lower limits in this sense. The main limitation of our analysis is that we have obtained total moment paleointensities rather than paleointensities for each component of magnetization. On the other hand, paleointensities derived from multicomponent and single component anomalies have median values that are well within our uncertainties (38 and 64 μT, respectively). We also note that a multicomponent NRM/sIRM study on bulk ALH 84001 grains [*Gattacceca and Rochette*, 2004] measured a characteristic

component paleointensity within a factor of 2 of our single component median paleointensity.

[18] We conclude that within the uncertainties of the NRM/sIRM method, our paleointensities are accurate indicators of the ancient Martian paleofield. This $\sim$50 μT field was most likely the product of either an active core dynamo or crustal magnetization that was the product of a previous dynamo that had since decayed. Even if such a field was responsible for magnetizing the Martian crust, the large intensity of the crustal anomalies would still have required surprisingly large concentrations of ferromagnetic minerals (perhaps 10 times that of the Earth's continents). Regardless of whether the field was of local or global extent, it would likely have shielded the local Martian atmosphere from loss due to impingement of the solar wind. The end of the early Martian dynamo may therefore have played an important role in climate change on Mars.

[19] **Acknowledgments.** We thank the NSF Geophysics and Instrumentation and Facilities Programs and the NASA Mars Fundamental Research and Planetary Major Equipment Programs (B.W.) and the Natural Science and Engineering Research Council (NSERC) of Canada (H.V.) for their support of this work. Two anonymous reviewers provided insightful comments that improved the manuscript.

References

Acuna, M., et al. (1999), Global distribution of crustal magnetization discovered by the Mars Global Surveyor MAG/ER experiment, *Science*, *284*, 790–793.

Antretter, M., and M. Fuller (2002), Paleomagnetism and rock magnetism of Martian meteorite ALH84001, *Phys. Chem. Earth*, *27*, 1299–1303.

Antretter, M., M. Fuller, E. Scott, M. Jackson, B. Moskowitz, and P. Solheid (2003), Paleomagnetic record of Martian meteorite ALH84001, *J. Geophys. Res.*, *108*(E6), 5049, doi:10.1029/2002JE001979.

Butler, R. F. (1972), Natural remanent magnetization and thermomagnetic properties of Allende meteorite, *Earth Planet. Sci. Lett.*, *17*, 120–128.

Collinson, D. W. (1997), Magnetic properties of Martian meteorites: Implications for an ancient Martian magnetic field, *Meteorit. Planet. Sci.*, *32*, 803–811.

Connerney, J., et al. (1999), Magnetic lineations in the ancient crust of Mars, *Science*, *284*, 794–798.

Fong, L. E., et al. (2005), High resolution room-temperature sample scanning superconducting interference device microscope configurable for geological and biomagnetic applications, *Rev. Sci. Instrum.*, *76*, 053703, doi:10.1063/1.1884025.

Gattacceca, J., and P. Rochette (2004), Toward a robust normalized magnetic paleointensity method applied to meteorites, *Earth Planet. Sci. Lett.*, *227*, 377–393.

Gattacceca, J., et al. (2005), An impact origin for the foliation of chondrites, *Earth Planet. Sci. Lett.*, *234*, 351–368.

Genge, M. J., and M. M. Grady (1999), The fusion crusts of stony meteorites: Implications for the atmospheric reprocessing of extraterrestrial materials, *Meteorit. Planet. Sci.*, *34*, 341–356.

Jull, A. J. T., et al. (1995), Isotopic composition of carbonates in the SNC meteorites Allan Hills 84001 and Nakhla, *Meteoritics*, *30*, 311–318.

Kirschvink, J. L., et al. (1997), Paleomagnetic evidence of a low-temperature origin of carbonate in the Martian meteorite ALH84001, *Science*, *275*, 1629–1633.

Rochette, P., et al. (2005), Matching Martian crustal magnetization and magnetic properties of Martian meteorites, *Meteorit. Planet. Sci.*, *40*, 529–540.

Selkin, P. A., et al. (2000), The effect of remanence anisotropy on paleointensity estimates: A case study from the Archean Stillwater Complex, *Earth Planet. Sci. Lett.*, *183*, 403–416.

Shuster, D. L., and B. P. Weiss (2005), Martian surface paleotemperatures from thermochronology of meteorites, *Science*, *309*, 594–597.

Steele, A., et al. (2007), Comprehensive imaging and Raman spectroscopy of carbonate globules from Martian meteorite ALH 84001 and a terrestrial analogue from Svalbard, *Meteorit. Planet. Sci.*, *9*, 1549–1566.

Sugiura, N., and D. W. Strangway (1983), A paleomagnetic conglomerate test using the Abee E4 meteorite, *Earth Planet. Sci. Lett.*, *62*, 169–179.

Watson, G. S. (1956), A test for randomness, *Mon. Not. R. Astron. Soc.*, *7*, 160–161.

Weiss, B. P., et al. (2000), A low temperature transfer of ALH84001 from Mars to Earth, *Science*, *290*, 791–795.

Weiss, B. P., et al. (2002a), Temperatures on Mars from ^{40}Ar/^{39}Ar thermochronology of ALH84001, *Earth Planet. Sci. Lett.*, *201*, 465–472.

Weiss, B. P., et al. (2002b), Records of an ancient Martian magnetic field in ALH84001, *Earth Planet. Sci. Lett.*, *201*, 449–463.

Weiss, B. P., et al. (2004), Magnetic tests for magnetosome chains in Martian meteorite ALH84001, *Proc. Natl. Acad. Sci. U. S. A.*, *101*, 8281–8284.

Weiss, B. P., et al. (2007a), Paleointensity of the Earth's magnetic field using SQUID microscopy, *Earth Planet. Sci. Lett.*, *264*, 61–71.

Weiss, B. P., E. A. Lima, L. E. Fong, and F. J. Baudenbacher (2007b), Paleomagnetic analysis using SQUID microscopy, *J. Geophys. Res.*, *112*, B09105, doi:10.1029/2007JB004940.

F. J. Baudenbacher and L. E. Fong, Department of Physics and Astronomy, Vanderbilt University, Nashville, TN 37235, USA.

E. A. Lima and B. P. Weiss, Department of Earth, Atmospheric, and Planetary Sciences, Massachusetts Institute of Technology, 54-814, Cambridge, MA 02139, USA. (bpweiss@mit.edu)

H. Vali, Department of Anatomy and Cell Biology, McGill University, Montréal, QC H3A 2B2, Canada.

Auxiliary material for Paper 2008GL035585

Paleointensity of the ancient Martian magnetic field

Benjamin P. Weiss
Department of Earth, Atmospheric, and Planetary Sciences, Massachusetts Institute of Technology, Cambridge, Massachusetts, USA

Luis E. Fong
Department of Physics and Astronomy, Vanderbilt University, Nashville, Tennessee, USA

Hojatollah Vali
Department of Anatomy and Cell Biology and Facility for Electron Microscopy Research, McGill University, Montreal, Quebec, Canada

Department of Earth and Planetary Sciences, McGill University, Montreal, Quebec, Canada

Eduardo A. Lima
Department of Earth, Atmospheric, and Planetary Sciences, Massachusetts Institute of Technology, Cambridge, Massachusetts, USA

Franz J. Baudenbacher
Department of Physics and Astronomy, Vanderbilt University, Nashville, Tennessee, USA

Department of Biomedical Engineering, Vanderbilt University, Nashville, Tennessee, USA

Weiss, B. P., L. E. Fong, H. Vali, E. A. Lima, and F. J. Baudenbacher (2008), Paleointensity of the ancient Martian magnetic field, Geophys. Res. Lett., 35, L23207, doi:10.1029/2008GL035585.

1. 2008GL035585-txts01.txt
1.0. Ferromagnetic mineralogy of ALH 84001.
2.0. The age and origin of the magnetization in ALH 84001.
3.0. Paleointensity method and its uncertainties.
4.0. Least squares analysis of NRM and AF demagnetization.
5.0. Vertical isothermal remanent magnetization acquisition.
6.0. Anisotropy of remanent magnetization.
References.
Endnotes.

2. 2008GL035585-ts01.txt
Table S1. Previous paleointensity estimates for ALH 84001. Shown are all previously published paleointensity estimates of ALH 84001 arranged in order of subsample mass. All studies measured the ratio of natural remanent magnetization (NRM) to saturation isothermal remanent magnetization (sIRM). The first and second columns are measurements, and the third column is computed by multiplying the data in the second column by a calibration factor of 3000.

3. 2008GL035585-ts02.txt
Table S2. Paleointensity estimates for ALH 84001 from this study. Shown are paleointensity estimates of ALH 84001 from each of 41 anomalies (see Supplementary Text). Column 1 lists the anomaly #, column 2 gives the mineralogy of the anomaly as inferred from electron microscopy and IRMz-acquisition data (Figs. S5, S6), columns

3 and 4 respectively give the natural remanent magnetization (NRM) and isothermal remanent magnetization at 545 mT (a close approximation of saturation isothermal remanent magnetization, sIRM), column 5 gives the ratio of the values in columns 3 and 4, and column 6 gives the inferred paleointensity in microteslas = (column 5) x a where a ~ 3000 is an empirically determined calibration factor (Fuller and Cisowski, 1987; Gattacceca and Rochette, 2004; Kletetschka et al., 2003; Kletetschka et al., 2004; Yu, 2006).

4. 2008GL035585-fs01.jpg
Figure S1. Previous paleointensity experiments on ALH 84001. Shown is the ratio of natural remanent magnetization to saturation isothermal remanent magnetization, NRM/sIRM, and the equivalent paleointensity in microteslas (3000 × NRM/sIRM, plotted as a function of sample mass used for the analyses. Data and references are in Supplementary Table 1. For the 0.4897 g sample of Antretter and Fuller [Antretter and Fuller, 2002], which exhibited a strong, reversed low-coercivity overprint, both the NRM/sIRM and that after alternating field demagnetization in a peak field of 20 mT, NRM(20 mT)/sIRM(20 mT), are plotted (white and grey circles, respectively).

5. 2008GL035585-fs02.jpg
Figure S2. Backscattered scanning electron microscopy (BSEM) imaging of ALH 84001. (A) BSEM image of ALH 84001,227b,2. Bright (dark) features correspond to high (low) atomic number elements. Locations of higher resolution images in C and D are shown. (B) BSEM image overlaid on SQUID Microscope image of natural remanent magnetism field (Fig. 1A). (C) High-resolution BSEM image of region labeled “C” in (A) showing zoned magnetite and pyrrhotite-bearing carbonate (center and top, mottled grey) and plagioclase glass (dark grey, bottom) surrounded by orthopyroxene (light grey). (D) High-resolution BSEM image of region labeled “D” in (A) showing two chromites (white) surrounded by orthopyroxene (light grey). Location of high-resolution image in (E) is shown. (E) Image of chromite in (D) with stretched grayscale showing that this grain is actually a composite of chromite (dark grey) and sulfide (light grey). Scale bars are 1 mm (A, B), 50 μm (C), 100 μm (D) and 25 μm (E). Accelerating voltage was 15 kV for (A, D, E) and 25 kV for (C).

6. 2008GL035585-fs03.jpg
Figure S3. Electron microscopy imaging of ultrathin section of ALH 84001 chromite (not associated with the 227b,2 thin section) prepared by focused ion beam milling using the Hitachi FB-2000A. (A) Backscatter scanning electron microscopy (BSEM) image showing chromite (dark) with fracture-filling sulfide (bright) running down center of image. (B) X-ray compositional maps showing Cr (B), Fe (C) and S (D) concentrations in region defined by dashed box in A. Scale bar for (A-D) is 1 μm. (E, F) High resolution transmission electron microscopy imaging of ultrathin section of ALH 84001 sulfide-bearing chromite shown in (A-D). Lattice-fringe images and diffraction patterns were obtained by the JEOL JEM-2100F FE-TEM at an accelerating voltage of 200 kV. Lattice fringes indicative of monoclinic pyrrhotite are labeled. Scale bars are 2 nm.

7. 2008GL035585-fs04.jpg
Figure S4. Locations of 41 anomalies in (A) NRM and (B) IRMz(545 mT) scans. Identification numbers used in text are labeled next to each anomaly.

8. 2008GL035585-fs05.jpg
Figure S5. Vertical isothermal remanent magnetization (IRMz) fields of ALH 84001,227b,2 during progressive exposure to vertical (out-of-the-page) fields. Shown is the vertical component of the field as measured 140 μm above the sample; positive (out-of-the-page) fields are red and yellow and negative (into-the-page) fields are blue. All images share 1 mm scale bar and intensity scale at right. (A) After a field of 20 mT. (B) After a field of 60 mT. (C) After a field of 100 mT. (D) After a field of 300 mT. (D) After a field of 450 mT. (E) After a field of 545 mT.

9. 2008GL035585-fs06.jpg
Figure S6. Vertical isothermal remanent magnetization (IRMz) acquisition by

individual magnetic anomalies in ALH 84001,227b,2. These IRMz values are inferred from unidirectional least squares fits to SQUID Microscope data (Fig. S5). (A) Selected IRMz acquisition plots for two carbonate-magnetite-sulfide anomalies (#2 and #5; diamonds), two chromite-sulfide anomalies (#4 and #8; squares), and the bulk sample (dominated by magnetite-bearing fusion crust; circles). Data are normalized to IRM after 545 mT [IRMz(545 mT)]. The three magnetite-bearing assemblages are saturated by 300 mT whereas the two chromite-sulfide assemblages saturate above 545 mT. (B) Histogram of IRMz for all analyzed anomalies. Each box represents the saturation field inferred from least squares fits to IRMz data for an individual numbered anomaly (see Fig. S4). White boxes = chromite-sulfide assemblages, light grey boxes = carbonate-magnetite-sulfide assemblages, and dark grey boxes = magnetite-bearing fusion crust.

10. 2008GL035585-fs07.jpg
Figure S7. Anisotropy of isothermal remanent magnetization (IRM) study on ALH 84001,227b,2 using SQUID microscopy. Shown is the vertical component of the IRM fields 140 μm above the sample following its exposure to nearly saturating fields oriented in three orthogonal directions. Positive (out-of-the-page) fields are red and yellow and negative (into-the-page) fields are blue. All images share intensity scale at right. Scale bars are 1 mm. (A) IRMz(545 mT) (vertical) field. (B) IRMx(545 mT) (horizontal toward top of page) field. (C) IRMy(540 mT) (horizontal toward page left) field.

11. 2008GL035585-fs08.jpg
Figure S8. Analysis of anisotropy of remanence data. Shown are the results of least squares fits to isothermal remanent magnetization fields in three orthogonal directions (data in Fig. S7). (A-C) Results of unidirectional least squares magnetization fits to anomaly #1 (see Fig. S4) after exposure to 545 mT fields oriented in the z (out-of-the-page) (A), x (toward top) (B) and y (toward left) (C) directions. Each equal area plot shows the residual root mean square (residual RMS) as a function of assumed magnetization direction for 100 directions distributed uniformly over the sphere. Contour intervals are 23.0 nT (A), 17.1 nT (B), and 10.3 nT (C). Shaded areas in each plot equals expected uncertainty for each fit (ascribed to position noise and the background field fields from surrounding unmodeled magnetic anomalies). Applied field directions are shown by red stars. The uncertainty for each of the applied fields directions is ~5-10°. (D-F) Equal area plots showing the aggregate residual RMS as a function of magnetization fit direction for all 41 magnetic anomalies in Fig. S4 for 545 mT fields applied in the z (D), x (E) and y (F) directions. Each plot is the sum of 41 individual anomaly residual RMS plots like those shown in A-C.

12. 2008GL035585-fs09.jpg
Figure S9. Direction of NRM during AF demagnetization of selected anomalies as inferred from least squares inversion of SQUID Microscope scans (main text Fig. 2). Closed (open) symbols represent equal area projections of anomaly directions onto lower (upper) hemisphere. Black circles = carbonate-magnetite-pyrrhotite and chromite-sulfide anomalies in meteorite deep interior, red pentagons = fusion crust, red circles = anomalies in baked zone. Star = resultant vector (mean) of all directions in each equal area plot (calculated as part of Watson's conglomerate test). (A) NRM. (B) After AF 5 mT. (C) After AF 10 mT. (D) After AF 20 mT. (E) After AF of 30 mT. (F) After AF 40 mT. (G) After AF 50 mT. (H) After AF 60 mT. (I) After AF 70 mT. (J) After AF 80 mT. (K) After AF 90 mT. (L) After peak AF of 99 mT.

13. 2008GL035585-fs10.jpg
Figure S10. Histograms of NRM/sIRMz measured for 41 anomalies. IRMz(545 mT) was used as an estimate of sIRMz. (A) Fusion crust and baked zone anomalies. (B) Unbaked (> 3 mm interior to fusion crust) anomalies. Dashed lines give median values for each distribution.

Auxiliary Text

1.0. Ferromagnetic mineralogy of ALH 84001. Determining the mineralogical sources of the magnetic anomalies observed in ALH 84001 is important for determining the mode and timing of remanence acquisition. Towards this end, we conducted backscattered electron microscopy (BSEM) imaging of the 227b,2 thin section following all magnetic analyses. These data were obtained using a high-resolution Robinson BSE detector on a Hitachi S-4700 field-emission scanning electron microscope. The analysis was performed on a polished, carbon-coated thin section at accelerating voltages of 25 kV and 15 kV and working distances of 12 and 24 mm.

The BSEM data indicate that the magnetic anomalies are associated with three macroscopic phases: fusion crust, carbonate, and chromite (Fig. S2). Although a similar association was noted in our previous study of thin section 227b,2 [Weiss et al., 2002b], the new data presented here, which have a resolution twice as fine as that of the previous study, greatly augment this observation. The first two of these sources were expected: carbonate in ALH 84001 contains both magnetite and pyrrhotite [Weiss et al., 2002b], and fusion crust in stony meteorites is usually magnetite-rich [Genge and Grady, 1999]. Our alternating field (AF) demagnetization of NRM and isothermal remanent magnetization (IRM) acquisition data (see below and Figs. 1, 4, S5, and S6) indicate that all carbonate- and fusion crust-associated anomalies have coercivities below 300 mT (characteristic of magnetite), whereas chromite-associated anomalies almost exclusively have coercivities greater than or equal to 300 mT.

The room-temperature NRM associated with ALH 84001 chromite has been a puzzle since it was first discovered [Weiss et al., 2002b]. A major problem with understanding this is that no magnetic properties have been reported for the exact composition of the ALH 84001 chromite ($Fe_{1.05}Cr_{1.31}Al_{0.35}Mg_{0.20}Ti_{0.06}O_{4.0}$ as calculated from the data of [Mittlefehldt, 1994]). However, studies of binary spinel solid solution series indicate that the increasing replacement of Fe in magnetite with Al, Mg and Ti tends to lower the Curie point and saturation magnetization. With this in mind, if we use $Fe_{1.05}Cr_{1.95}O_4$ as a model (chosen because it is one of the spinel compositions closest in composition to ALH 84001 chromite whose magnetic properties are well-known), we would predict a Curie point of only ~90 K. In fact, magnetic studies of bulk grains and chromite separates suggest that ALH 84001 chromite has a dominant Curie point of almost exactly this temperature [Antretter et al., 2003; Weiss et al., 2004]. This would seem to indicate that the chromite should only be paramagnetic at room temperature.

Our high resolution BSEM images of many ALH 84001 chromites associated with magnetic anomalies have detected no exsolution textures which could be candidate ferromagnetic minerals with greater than room-temperature Curie points. Instead, we found that chromite is very often intimately associated with iron sulfide. Such an association has been previously noted [Greenwood et al., 2000; Mittlefehldt, 1994]. To examine this further, we conducted transmission electron microscopy (TEM) imaging of an ultrathin section extracted from ALH 84001 chromite using focused ion-beam milling (Fig. S3). The section was prepared from an isolated chromite grain (not associated with the 227b,2 thin section) using a Hitachi FB-2000A focused ion beam system. This TEM investigation once again did not find exsolution features but did find small amounts of iron sulfide in the interior of the chromite. This sulfide has lattice fringes of of 0.29 nm (220, 400), 0.26 nm (4-overbar 04, 2-overbar 24) or (224, 404), 0.21 nm (2-overbar 28) or (228), 0.17 nm (040, 620), 0.15 nm (440, 800), and 0.48 and 0.46 nm (1-overbar 13), characteristic of the ferromagnetic mineral monoclinic pyrrhotite [JCPDS, 1980; Morimoto et al., 1975].

If this pyrrhotite is the source of the chromite room-temperature NRM, then how can we explain the apparent 90 K Curie point? Although the saturation magnetization of spinels with the exact composition of those in ALH 84001 has not been measured, if it is similar to $Fe_{1.05}Cr_{1.95}O_4$, then it would be within a factor of ~2-3 of pyrrhotite. Therefore, that fact that our electron microscopy observations indicate that associated pyrrhotite typically makes up

no more than a few percent of the mass of surrounding chromite would explain why there is little evidence of pyrrhotite during our previous low-temperature magnetic studies of chromite separates [Weiss et al., 2004]1. Such a pyrrhotite abundance can account for the observed room-temperature NRM intensities assuming NRM/sIRM ~ 1%. In summary, there appear to be two main mineralogical carriers of magnetization in ALH 84001: magnetite (dominating the fusion crust and carbonate) and pyrrhotite intimately spatially associated with carbonate and chromite.

2.0. The age and origin of the magnetization in ALH 84001. There are a wide range of constraints on the timing of NRM acquisition for ALH 84001. The magnetite-pyrrhotite-carbonate assemblages formed sometime between 4.14-3.86 Ga [Borg et al., 1999] and the chromite-sulfide assemblages probably formed at the 4.5 Ga crystallization age of the bulk meteorite [Jagoutz et al., 1994; Nyquist et al., 1995]. These ages are upper limits on the age of the magnetization carried by these phases.

In fact, ALH 84001 has experienced a violent history, with at least one and possibly multiple shock event(s) that occurred during and/or after the formation of the free sulfides and carbonate and that produced diaplectic glass [Greenwood and McSween, 2001; Treiman, 1998]. Petrographic data indicate most of the glass and nearby carbonate reached peak shock pressures of ~32 GPa, peak-shock temperatures of ~30-150°C, and post-shock temperatures of ~14-40°C, although the presence of rare vesicles suggests that small (sub-cm) regions reached pressures >45 GPa with post-shock temperatures of several hundred °C [Artemieva and Ivanov, 2004; Baer, 1999; Barber and Scott, 2006; Bischoff and Stoffler, 1992; Cooney et al., 1999; Fritz et al., 2005a; Fritz et al., 2005b; Kring et al., 1998; Treiman, 1998]. Some authors have argued that one of these shock events actually formed some [Eiler et al., 2002] or all [Barber and Scott, 2003; 2006] of the carbonate-magnetite assemblages from shock-melts, or at least formed the magnetite within pre-existing carbonate [Bell, 2007; Golden et al., 2004; Treiman, 2003]. Regardless of the details, these shock event(s) must have partially remagnetized at least localized (millimeter to submillimeter scale) regions of the meteorite2. There are two ways these shock events could have produced the heterogeneous pattern of magnetization. The first is via rotation of grains due to shock brecciation, which would involve no remagnetization of the individual grains [Greenwood and McSween, 2001]. The second is via spatially nonuniform heating by multiple shock events, which could heterogeneously remagnetize the rock at fine scales. The latter process could produce varying magnetization directions if (a) during the impacts the rock rotated while the field remained steady and/or if (b) the rock remained stationary during the impacts but the field itself changed during the intervals between the shock events.. Note that heterogeneous heating at submillimeter scales is a well-known aspect of shock events that has been observed both experimentally and theoretically in a wide variety of natural materials [Baer, 1999; Bischoff and Stoffler, 1992; Malavergne et al., 2001] including ALH 84001 [Treiman, 1998]. On the other hand, our proposal that this process could produce heterogeneously oriented magnetization has yet to be experimentally verified.

In any case, the persistence of this nonunidirectional magnetization suggests that the meteorite has been well below the Curie point of magnetite (580°C) since the last major shock event. Weiss et al. [Weiss et al., 2000] further argued that the meteorite was cooler than 40-80°C during ejection from Mars. However, the subsequent realization that magnetite makes a significant contribution to the NRM [Antretter et al., 2003; Rochette et al., 2005; Weiss et al., 2002b] means that the magnetization at these blocking temperatures is more susceptible to viscous remanent magnetization (VRM) than originally thought (magnetite and pyrrhotite in ALH 84001 should have been viscously remagnetized up to 1 hour blocking temperatures of ~150°C and 80°C [Weiss et al., 2000]). Regardless, the results of Weiss et al. [Weiss et al., 2000] are remarkably consistent with the previously mentioned shock petrographic constraints [Fritz et al., 2005a; Fritz et al., 2005b].

A variety of other datasets on ALH84001 strongly indicate that at least no long-term heating above the magnetite Curie point has occurred since 4 Ga. The

meteorite has an 40Ar/39Ar age of 3.9-4.3 Ga [Bogard and Garrison, 1999]. 40Ar/39Ar thermochronology calculations [Shuster and Weiss, 2005; Weiss et al., 2002a], 4 Ga U/Pb apatite ages [Terada et al., 2003], cation zoning in carbonate [Fisler and Cygan, 1998; Kent et al., 2001], and Fe2+ -Mg ordering in orthopyroxene [Domeneghetti et al., 2007] collectively indicate that much of the meteorite was heated to >500°C at 4 Ga but has not since been warmer than 350-500°C except possibly for very brief intervals (hours). The 40Ar/39Ar and new (U-Th)/He data [Min and Reiners, 2007] in particular indicate it was not heated above 350-400°C during ejection from Mars and transfer to Earth (despite the title of [Min and Reiners, 2007], both studies have placed nearly identical upper limits on the temperature experienced by ALH 84001 during ejection). Finally, [Barber and Scott, 2003] argue that the lack of major shock deformational features in the carbonate indicates that they have not been shock-heated above ~500°C since minutes after they formed. These data collectively strongly indicate there has been no long term heating of ALH 84001 above the magnetite Curie point since ~4 Ga and are consistent with the characteristic magnetization being acquired as a thermoremanence (TRM) at that time. Previous AF demagnetization studies of bulk ALH 84001 grains [Antretter et al., 2003; Collinson, 1997; Gattacceca and Rochette, 2004] demonstrate that this TRM was overprinted by one or more secondary components at more recent but not well-determined time(s). We do not favor the overprint as a crystallization remanent magnetization given the near complete lack of post-carbonate weathering minerals in the meteorite; although it is possible that hematite in carbonates is an alteration product of magnetite, [Steele et al., 2007] favor hematite as a primary depositional phase and TEM [Weiss et al., 2002b] and our IRM acquisition data (Section 5.0 and Fig. S6) suggest that hematite is significantly less abundant than magnetite. There is no evidence of secondary low-field IRM in the multicomponent paleointensity experiment of [Gattacceca and Rochette, 2004]. The three most likely secondary overprints in ALH 84001 are (a) low-temperature impact-related partial TRM (b) a partial shock remanent magnetization (SRM) (e.g., [Cisowski and Fuller, 1978]) in moderately shocked (< 30 GPa) regions of the meteorite, and (c) a VRM acquired on Earth. If an SRM is present, it does not invalidate our paleointensity estimates but rather means they are likely lower limits due to the inefficiency of SRM relative to thermoremanent magnetization (TRM) [Gattacceca et al., 2008; Pohl and Eckstaller, 1981]. However, the possibility of impact-generated magnetic fields [Carporzen et al., 2005; Crawford and Schultz, 1999; Srnka et al., 1979] would mean that SRM and impact-related TRM may not record internally generated Martian fields.3

In summary, the weight of the evidence suggests that at least the characteristic magnetization in ALH 84001 is likely a TRM dating back to at least 4 Ga which has been subsequently partially overprinted. The fact that the within-sample anomaly NRM directions (Fig. S9) do not plot along a great circle would indicate that there must have been at least two such remagnetizing events after carbonate formation. Future magnetic microscopy paleointensity studies of ALH 84001 should therefore employ multicomponent paleointensity techniques.

3.0. Paleointensity method and its uncertainties. It has been demonstrated from studies of a wide variety of terrestrial and extraterrestrial minerals (including both magnetite and pyrrhotite) and their synthetic analogs that for low-field TRM (<10% of sIRM), the ratio of TRM to sIRM is roughly proportional to the intensity of the paleofield which produced the TRM [Fuller and Cisowski, 1987; Fuller et al., 1988; Fuller et al., 2002; Gattacceca and Rochette, 2004; Kletetschka et al., 2003; Kletetschka et al., 2004; Kletetschka et al., 2006; Verrier and Rochette, 2002]. Samples containing approximately equant crystal shapes will have TRM/sIRM ~ several % for a single TRM component produced in Earth’s field (~50 μT), although extreme acicular shape distributions can have TRM/sIRM that is 50 times higher than that of equant grains [Yu et al., 2007]. For samples without such extreme shape distributions, the paleointensity estimate from this technique has an uncertainty of a factor of up to ~10 (for extremely narrow size distributions) and more typically ~2-5 (for samples with fairly uniform size distributions), with the chief sources of error being the dependence of TRM intensity on the unknown grain volume and microscopic coercivity distribution [Lawrence et al., 2008; Yu, 2006].

Paleointensities of samples with multiple components (see Section 2.0) computed using the ratio of total NRM to total sIRM will provide only a lower limit on the average paleointensity of all components and as a result will not isolate the characteristic component, which is often the easiest to identify as a thermoremanence. This inability to distinguish paleointensities of individual components is the chief limitation of this study and makes it complementary to the multicomponent analysis of [Gattacceca and Rochette, 2004].

To summarize, we calculated the paleointensities in Supplementary Table 2 using the following formula: Paleointensities in microteslas = NRM/IRMz(545 mT) × 3000. Because the ratio of TRM to IRM is nonlinear when TRM/IRM > ~10% [Kletetschka et al., 2006], the IRM paleointensity technique is not well-calibrated for such efficiently magnetized samples and we do not report paleointensities for the one anomaly in this category.

4.0. Least squares analysis of NRM and AF demagnetization. The basis of our least squares fits for magnetization are described in detail elsewhere [Weiss et al., 2007a; b]. Unlike basalt samples previously studied using SQUID microscopy, on the cm-scale ALH 84001 has localized and nonunidirectional rather than continuous, unidirectional magnetization. However, because the meteorite's magnetization direction is not controlled by anisotropy (see Section 6.0), we can infer that at some smaller spatial scale the magnetization should be unidirectional.

To determine whether such a scale was resolved by the SM, we selected 41 subregions of the full SM scans and applied unidirectional least squares fits to each region. Each of these 41 anomalies are analogous to the magnetized seamounts mapped by ship-borne magnetometers as described by Parker [Parker, 1991]. With respect to seamount inversions, we have the critical advantage that we can bound the locations of magnetic sources by remagnetizing the entire thin section in a known direction. As such, we began by fitting unidirectional fits to our vertical isothermal remanent magnetization (IRMz) maps (see below and Fig. S6). The locations of these sources were then fixed at the same locations for the inversions of the NRM and AF demagnetization maps.

We estimate that the two main sources of uncertainty in our least squares fits to each anomaly are (i) position noise due to imprecise knowledge of the exact location of each field datum [Lee et al., 2004; Weiss et al., 2007a], and (ii) fields from surrounding unmodeled anomalies (e.g., [Parker et al., 1987; Parker, 1991]). The strongest anomalies will tend to be dominated by position noise while weaker anomalies (particularly those near the strongly magnetized fusion crust) will tend to be dominated by fields from unmodeled anomalies. Unfortunately, it is difficult to obtain precise estimates of the latter error because the magnetization pattern around any particular anomaly is not known a priori. Using the equations for position noise above dipoles in [Lee et al., 2004] and qualitatively estimating the intensity of background unmodeled fields, we found that the fit magnetization directions for most anomalies had uncertainties of ~10-50°. Although this angular uncertainty is large by the standards of moment magnetometry, it still is sufficiently small that we can argue that (a) the anomalies outside the baked zone are randomly magnetized, and (b) anomalies in the baked zone are mainly magnetized downward-west and fail the Watson conglomerate test (see main text).

We can also use the uncertainty estimates to test the hypothesis that the ALH 84001 anomalies are unidirectionally magnetized by comparing the residuals from our unidirectional least squares fits with the expected measurement noise. We found that fits to most anomalies indeed had residuals that did not exceed this noise level, consistent with the hypothesis that they are unidirectional. However, inversions on several anomalies (e.g., #21, #22, and #26) had residuals that well exceeded our measurement noise, indicating that those anomalies themselves cannot be unidirectional. For these anomalies, the fit NRM will be a lower limit on the true microscale magnetization, while the fit directions (Fig. S9) are highly uncertain

5.0. Vertical isothermal remanent magnetization acquisition. Our least squares analyses of the 41 magnetic anomalies during stepwise IRMz-acquisition (Fig. S5) found that the magnetization of most anomalies increased monotonically in

intensity with applied field and rapidly oriented unidirectionally toward the applied field direction. Anomalies associated with carbonate and fusion crust saturated by ~300 mT (as expected for their magnetite-dominated mineralogy), whereas anomalies associated with chromite-sulfide assemblages continued to acquire magnetization at 450 mT and higher fields (Fig. S6). This provides independent support for our electron microscopic identification of pyrrhotite described above. These IRM-acquisition studies, the first conducted using SQUID microscopy, demonstrate how rock magnetic properties can be mapped across a thin section to deduce the mineralogy of individual magnetic anomalies at submillimeter scales. They provide additional support for the mineralogical identifications for each anomaly, which previously were based only on a spatial correlation between NRM and compositional (electron and optical microscopy) maps.

6.0. Anisotropy of remanent magnetization. We also conducted the first anisotropy of remanence studies using SQUID microscopy. These studies were motivated by the hypothesis [Antretter et al., 2003; Barber and Scott, 2003] that the heterogeneous orientation of magnetization in ALH 84001 could be the product of fine-scale magnetic remanence anisotropy. If true, this would indicate that the meteorite has a fine-scale anisotropy that is so intense it would (a) likely invalidate our paleomagnetic conglomerate test (see main text), and (b) require that our raw paleointensity estimates be multiplied by a correction factor that depends on the degree of anisotropy for each anomaly [Selkin et al., 2000].

We used a comparison of our IRMx(545 mT), IRMy(545 mT) and IRMz(545 mT) field maps (Fig. S7) to test for such anisotropy. Our least squares fits found that the magnetization directions of all 41 individual anomalies had IRM orientations indistinguishable from the applied field direction for all three IRM directions (Fig. S8). Also, for all 41 anomalies, the intensities of IRMx(545 mT), IRMy(545 mT) and IRMz(545 mT) were indistinguishable for each anomaly. Because our inversions yielded moments with fairly high uncertainties (up to several tens of % in magnitude and up to several tens of degrees in direction), this is not a very sensitive test of anisotropy (certainly, it does not justify computing an anisotropy tensor [Hrouda, 1982] for each anomaly). Nevertheless, even with these uncertainties, the near spherical distribution of NRM and AF of NRM vectors (Fig. S9) cannot be explained as being primarily the result of magnetic anisotropy, which even at its most intense should restrict directions to a hemisphere. We conclude that magnetic anisotropy does not invalidate the conglomerate test. Given the uncertainties of the NRM/sIRM method (see Section 3.0), we did not correct our paleointensity estimates for anisotropy of remanence.

References

Antretter, M., and M. Fuller (2002), Paleomagnetism and rock magnetism of martian meteorite ALH84001, Phys. Chem. Earth, 27, 1299-1303.

Antretter, M., et al. (2003), Paleomagnetic record of Martian meteorite ALH84001, J. Geophys. Res., 108, doi: 10.1029/2002JE001979.

Artemieva, N., and B. Ivanov (2004), Launch of martian meteorites in oblique impacts, Icarus, 171(1), 84-101.

Baer, M. R. (1999), Computational modeling of heterogeneous reactive materials at the mesoscale, paper presented at Eleventh Conference on Shock Compression of Condensed Matter, American Institute of Physics, Snowbird, Utah.

Barber, D. J., and E. R. D. Scott (2003), Tranmission electron microscopy of minerals in the martian meteorite Allan Hills 84001, Meteorit. Planet. Sci., 38, 831-848.

Barber, D. J., and E. R. D. Scott (2006), Shock and thermal history of Martian meteorite Allan Hills 84001 from transmission electron microscopy, Meteorit. Planet. Sci., 41, 643-662.

Bell, M. S. (2007), Experimental shock decomposition of siderite and the origin of magnetite in Martian meteorite ALH 84001, Meteorit. Planet. Sci., 42, 935-949.

Bischoff, A., and D. Stoffler (1992), Shock metamorphism as a fundamental process in the evolution of planetary bodies: Information from meteorites, Eur.

J. Mineral., 4, 707-755.
Bogard, D. D., and D. H. Garrison (1999), Argon-39-argon-40 "ages" and trapped argon in Martian shergottites, Chassigny, and Allan Hills 84001, Meteorit. Planet. Sci., 34, 451-473.
Borg, L. E., et al. (1999), The age of the carbonates in martian meteorite ALH84001, Science, 286(5437), 90-94.
Carporzen, L., et al. (2005), Palaeomagnetism of the Vredefort meteorite crater and implications for craters on Mars, Nature, 435, 198-201.
Cisowski, S. M., and M. Fuller (1978), The effect of shock on the magnetism of terrestrial rocks, J. Geophys. Res., 83, 3441-3458.
Collinson, D. W. (1997), Magnetic properties of Martian meteorites - Implications for an ancient Martian magnetic field, Meteorit. Planet. Sci., 32, 803-811.
Cooney, T., et al. (1999), Vibrational spectroscopic study of minerals in the Martian meteorite ALH84001, Am. Mineral., 84, 1569-1576.
Crawford, D. A., and P. H. Schultz (1999), Electromagnetic properties of impact-generated plasma, vapor and debris, Int. J. Impact. Eng., 23, 169-180.
Domeneghetti, M. C., et al. (2007), Thermal history of ALH 84001 meteorite by Fe2+-Mg ordering in orthopyroxene, Meteorit. Planet. Sci., 42, 1703-1710.
Eiler, J. M., et al. (2002), Two populations of carbonate in ALH84001: Geochemical evidence for discrimination and genesis, Geochim. Cosmochim. Acta, 66, 1285-1303.
Fisler, D. K., and R. T. Cygan (1998), Cation diffusion in calcite: Determining closure temperatures and the thermal history for the Allan Hills 84001 meteorite, Meteorit. Planet. Sci., 33, 785-789.
Fritz, J., et al. (2005a), Ejection of martian meteorites, Meteorit. Planet. Sci., 40, 1393-1411.
Fritz, J., et al. (2005b), Micro-Raman spectroscopy of plagioclase and maskelynite in Martian meteorites: Evidence of progressive shock metamorphism, Antarct. Meteorite Res., 18, 96-116.
Fuller, M., and S. M. Cisowski (1987), Lunar paleomagnetism, in Geomagnetism, edited by J. A. Jacobs, pp. 307-455, Academic Press, Orlando.
Fuller, M., et al. (1988), NRM:IRM(s) demagnetization plots; an aid to the interpretation of natural remanent magnetization, Geophys. Res. Lett., 15, 518-521.
Fuller, M., et al. (2002), AF demagnetization characteristics of NRM, compared with anhysteretic and saturation isothermal remanence: an aid in the intrepretation of NRM, Phys. Chem. Earth, 27, 1169-1177.
Gattacceca, J., and P. Rochette (2004), Toward a robust normalized magnetic paleointensity method applied to meteorites, Earth Planet. Sci. Lett., 227, 377-393.
Gattacceca, J., et al. (2008), On the efficiency of shock magnetization processes, Phys. Earth. Planet. Inter., 166, 1-10.
Genge, M. J., and M. M. Grady (1999), The fusion crusts of stony meteorites: Implications for the atmospheric reprocessing of extraterrestrial materials, Meteorit. Planet. Sci., 34, 341-356.
Golden, D. C., et al. (2004), Evidence for exclusively inorganic formation of magnetite in Martian meteorite ALH84001, Am. Mineral., 89, 681-695.
Greenwood, J. P., et al. (2000), Sulfur isotopic compositions of individual sulfides in Martian meteorites ALH84001 and Nakhla: implications for crust-regolith exchange on Mars, Earth And Planetary Science Letters, 184(1), 23-35.
Greenwood, J. P., and H. Y. McSween (2001), Petrogenesis of Allan Hills 84001: Constraints from impact-melted feldspathic and silica glasses, Meteorit. Planet. Sci., 36, 43-61.
Hrouda, F. (1982), Magnetic anisotropy of rocks and its application in geology and geophysics, Geophys. Surv., 5, 37-82.
Jagoutz, E., et al. (1994), ALH84001: Alien or progenitor of the SNC family?, Meteoritics, 29, 478-479.
JCPDS (1980), Mineral Powder Diffraction File Data Book, 796 pp., International Center for Diffraction Data, Swarthmore, PA.
Kent, A. J. R., et al. (2001), The temperature of formation of carbonate in Martian meteorite ALH84001: Constraints from cation diffusion, Geochim. Cosmochim. Acta, 65, 311-321.

Kirschvink, J. L., et al. (1997), Paleomagnetic evidence of a low-temperature origin of carbonate in the Martian meteorite ALH84001, Science, 275, 1629-1633.
Kletetschka, G., et al. (2003), Magnetic remanence in the Murchison meteorite, Meteorit. Planet. Sci., 38, 399-405.
Kletetschka, G., et al. (2004), An empirical scaling law for acquisition of thermoremanent magnetization, Earth Planet. Sci. Lett., 226, 521-528.
Kletetschka, G., et al. (2006), TRM in low magnetic fields: a minimum field that can be recorded by large multidomain grains, Phys. Earth. Planet. Inter., 154, 290-298.
Kring, D. A., et al. (1998), Formation and relative ages of maskelynite and carbonate in ALH84001, Geochim. Cosmochim. Acta, 62, 2155-2166.
Lawrence, K., et al. (2008), Lunar paleointensity measurements: Implications for lunar magnetic evolution, Phys. Earth Planet. Inter., doi:10.1016/j.pepi.2008.1005.1007.
Lee, S.-Y., et al. (2004), Position noise in scanning superconducting quantum interference device microscopy, Appl. Phys. Lett., 84, 5001-5003.
Malavergne, V., et al. (2001), Description of new shock-induced phases in the Shergotty, Zagami, Nakhla and Chassigny meteorites, Meteorit. Planet. Sci., 36, 1297-1305.
Min, K., and P. W. Reiners (2007), High-temperature Mars-to-Earth transfer of meteorite ALH84001, Earth Planet. Sci. Lett., 260, 72-85.
Mittlefehldt, D. W. (1994), ALH84001, a cumulate orthopyroxenite member of the Martian meteorite clan, Meteoritics, 29, 214-221.
Morimoto, N., et al. (1975), Crystallography and stability of pyrrhotites, Econ. Geol., 70, 824-833.
Nyquist, L. E., et al. (1995), "Martians" young and old: Zagami and ALH84001, Lunar Planet. Sci. XXVI, 1065-1066.
Parker, R. L., et al. (1987), The application of inverse theory to seamount magnetism, Rev. Geophys., 25, 17-40.
Parker, R. L. (1991), A theory of ideal bodies for seamount magnetism, J. Geophys. Res., 96, 16101-16112.
Pohl, J., and A. Eckstaller (1981), The effect of shock on remanence in multi-domain iron grains and implications for paleointensity measurements, Lunar Planet. Sci. 12, 851-853.
Rochette, P., et al. (2005), Matching Martian crustal magnetization and magnetic properties of Martian meteorites, Meteorit. Planet. Sci., 40, 529-540.
Selkin, P. A., et al. (2000), The effect of remanence anisotropy on paleointensity estimates: a case study from the Archean Stillwater Complex, Earth Planet. Sci. Lett., 183, 403-416.
Shuster, D. L., and B. P. Weiss (2005), Martian surface paleotemperatures from thermochronology of meteorites, Science, 309, 594-597.
Srnka, L. J., et al. (1979), Magnetic field and shock effects and remanent magnetization in a hypervelocity impact experiment, Earth Planet. Sci. Lett., 42, 127-137.
Steele, A., et al. (2007), Comprehensive imaging and Raman spectroscopy of carbonate globules from Martian meteorite ALH 84001 and a terrestrial analogue from Svalbard, Meteorit. Planet. Sci., 9, 1549-1566.
Terada, K., et al. (2003), Ion microprobe U-Th-Pb dating of phosphates in Martian meteorite ALH 84001, Meteorit. Planet. Sci., 38, 1697-1703.
Treiman, A. H. (1998), The history of Allan Hills 84001 revised: Multiple shock events, Meteorit. Planet. Sci., 33, 753-764.
Treiman, A. H. (2003), Submicron magnetite grains and carbon compounds in Martian meteorite ALH84001: Inorganic, abiotic formation by shock and thermal metamorphism, Astrobiology, 3, 369-392.
Vaughan, D. J. (1978), Sulfide phase equilibria, in Mineral chemistry of metal sulfides, edited by D. J. Vaughan and J. R. Craig, p. 493, Cambridge University Press, Cambridge.
Verrier, V., and P. Rochette (2002), Estimating peak currents at ground lightning impacts using remanent magnetization, Geophys. Res. Lett., 29(18), art. no.-1867.
Weiss, B. P., et al. (2000), A low temperature transfer of ALH84001 from Mars to Earth, Science, 290, 791-795.
Weiss, B. P., et al. (2002a), Temperatures on Mars from 40Ar/39Ar

thermochronology of ALH84001, Earth Planet. Sci. Lett., 201, 465-472.
Weiss, B. P., et al. (2002b), Records of an ancient Martian magnetic field in ALH84001, Earth Planet. Sci. Lett., 201, 449-463.
Weiss, B. P., et al. (2004), Magnetic tests for magnetosome chains in Martian meteorite ALH84001, Proc. Natl. Acad. Sci. USA, 101, 8281-8284.
Weiss, B. P., et al. (2007a), Paleomagnetic analysis using SQUID microscopy, J. Geophys. Res., 112, B09105, doi:09110.01029/02007JB004940.
Weiss, B. P., et al. (2007b), Paleointensity of the Earth's magnetic field using SQUID microscopy, Earth Planet. Sci. Lett., 264, 61-71.
Yu, Y., et al. (2007), A linear field dependence of thermoremanence in low magnetic fields, Earth Planet. Sci. Lett., 162, 244-248.
Yu, Y. J., and J. S. Gee (2005), Spinel in Martian meteorite SaU 008: Implications for Martian magnetism, Earth Planet. Sci. Lett., 232, 287-294.
Yu, Y. J. (2006), How accurately can NRM/SIRM determine the ancient planetary magnetic field intensity?, Earth Planet. Sci. Lett., 250, 27-37.

Endnotes

1. We note that although Yu and Gee [Yu, Y. J., and J. S. Gee (2005), Spinel in Martian meteorite SaU 008: Implications for Martian magnetism, Earth Planet. Sci. Lett., 232, 287-294.] discounted pyrrhotite in favor of spinel as a possible source for room-temperature NRM in another Martian meteorite, it is possible that small amounts of included pyrrhotite could also have been missed during their low-temperature studies for the same reason. Their reported compositions for the free sulfides in the meteorite are marginally consistent with an intergrown mixture of very small amount of monoclinic pyrrhotite with hexagonal pyrrhotite [Vaughan, D. J. (1978), Sulfide phase equilibria, in Mineral chemistry of metal sulfides, edited by D. J. Vaughan and J. R. Craig, p. 493, Cambridge University Press, Cambridge.]

2. Note that this scenario differs from that of [Kirschvink et al., 1997], who argued that all carbonates had not been heated > 110°C during and since formation. The latter study predates much of the previously cited work that essentially requires that at least some carbonates were heated during and/or after their formation.

3. We consider it unlikely that the heterogeneous magnetization was produced in a way analogous to that invoked for cm-scale magnetization heterogeneity in the Vredefort impact crater, South Africa [Carporzen, L., et al. (2005), Palaeomagnetism of the Vredefort meteorite crater and implications for craters on Mars, Nature, 435, 198-201.]; the latter proposal invokes intense impact-plasmas produced locally within the host rock that created SRM near saturation. ALH 84001 does not show evidence for such high shock pressures, its magnetization is heterogeneous at even finer scales than that typically observed at Vredefort, and the NRMs of individual anomalies are on average only just a few percent of saturation IRM (Table S2).

Mass (mg)	NRM/sIRM (%)	Paleointensity (μT)	Reference
5000	0.182	5.5	Collinson, 1997
4500	0.187	5.6	Collinson, 1997
489.7	0.09*	2.7	Antretter et al., 2003
209	0.512†	21	Gattacceca and Rochette, 2004
12.7	2.70	81	Kirschvink et al., 1997
2.2	3.57	107	Kirschvink et al., 1997

*This sample exhibited an anomalously strong reversed low-coercivity overprint. For comparison with the other studies,

probably the remaining NRM and sIRM after alternating field (AF) demagnetization to a peak field of 12 mT, NRM(12 mT) and

sIRM(12 mT), should be used to estimate the normalized paleointensity. In that case, NRM(12 mT)/sIRM(12 mT) = 0.2%. If the

reversed component actually had the same direction as the higher coercivity magnetization, then the NRM/sIRM ~ 4%.

† The authors of this study (Gattacceca and Rochette, 2004) report both NRM/sIRM = 0.512% as well as its derivative with

respect to peak field (REM′) = 0.7%.

Anomaly	Mineralogy	NRM (Am2)	sIRMz (Am2)	NRM/sIRMz (%)	Paleointensity (μT)
1	chr-sulf	3.8e10-13	4.1e10-11	0.93	28
2	carb-mt-pyr	4.4e10-13	1.1e10-10	0.40	12
3*	fusion crust	2.2e10-11	1.6e10-9	1.4	41
4	chr-sulf	9.7e10-12	7.6e10-10	1.3	38
5	carb-mt-pyr	1.7e10-12	2.2e10-11	7.4	230
6*	carb-mt-pyr	2.1e10-12	1.5e10-10	1.4	42
7*	carb-mt-pyr	5.8e10-13	1.1e10-10	0.53	16
8*	chr-sulf	8.4e10-13	1.2e10-10	0.70	21
9	chr-sulf	5.0e10-12	8.1e10-10	0.62	19
10	carb-mt-pyr	2.4e10-13	5.3e10-13	45	**
11	chr-sulf	3.0e10-13	1.5e10-11	2.0	60
12	chr-sulf	3.7e10-13	2.9e10-11	1.3	38
13	chr-sulf?	2.2e10-12	3.0e10-10	0.73	22
14*	fusion crust	6.2e10-10	6.4e10-8	0.97	29
15*	carb-mt-pyr	3.5e10-11	2.7e10-9	1.30	39
16*	chr-sulf	6.9e10-13	9.0e10-11	0.77	23
17	chr-sulf	5.2e10-12	2.2e10-10	2.4	71
18*	chr-sulf	9.6e10-13	8.9e10-11	1.1	32
19	carb-mt-pyr	9.1e10-13	1.1e10-11	8.3	250
20	carb-mt-pyr	3.1e10-13	8.9e10-11	0.35	10
21	chr-sulf	1.8e10-12	1.8e10-11	10	300
22	chr-sulf	6.9e10-13	7.0e10-11	0.99	30
23*	chr-sulf	5.9e10-13	9.4e10-11	0.54	19
24	carb-mt-pyr	1.3e10-13	8.2e10-12	1.6	48
25	chr-sulf	2.3e10-13	1.8e10-11	1.3	38
26	chr-sulf	7.0e10-13	2.6e10-10	0.27	8.1
27	carb-mt-pyr?	2.8e10-13	4.0e10-12	7.0	210
28	chr-sulf	7.6e10-14	3.4e10-12	2.2	67
29	chr-sulf	1.7e10-12	6.8e10-11	2.5	75
30	chr-sulf	2.7e10-13	1.8e10-11	1.5	45
31*	chr-sulf	5.4e10-13	6.4e10-11	0.84	25
32*	chr-sulf	2.0e10-12	1.9e10-10	1.05	32
33*	carb-mt-pyr	4.4e10-13	3.8e10-11	1.2	35
34*	carb-mt-pyr	2.5e10-13	9.2e10-12	2.7	82
35*	carb-mt-pyr	4.7e10-13	2.8e10-11	1.7	50
36	carb-mt-pyr	3.0e10-13	4.0e10-12	7.5	230
37	chr-sulf	9.2e10-13	1.5e10-10	0.61	18
38*	chr-sulf	2.9e10-13	1.2e10-11	2.4	73
39*	chr-sulf	2.0e10-13	1.1e10-11	1.8	55
40	carb-mt-pyr	7.4e10-14	3.8e10-12	2.0	58
41	carb-mt-pyr	4.3e10-14	1.3e10-12	3.3	99

*Denotes anomalies associated with fusion crust or within 3 mm of the fusion crust (e.g., the baked zone). The median paleointensity of baked and fusion-crust associated anomalies is 34 μT and the median paleointensity of interior anomalies is 46 μT.

**Because the NRM/sIRM paleointensity method is not well-calibrated above NRM/sIRM~10% (beyond which the ratio of TRM to sIRM is nonlinear and poorly calibrated), we cannot report paleointensities for such anomalies.

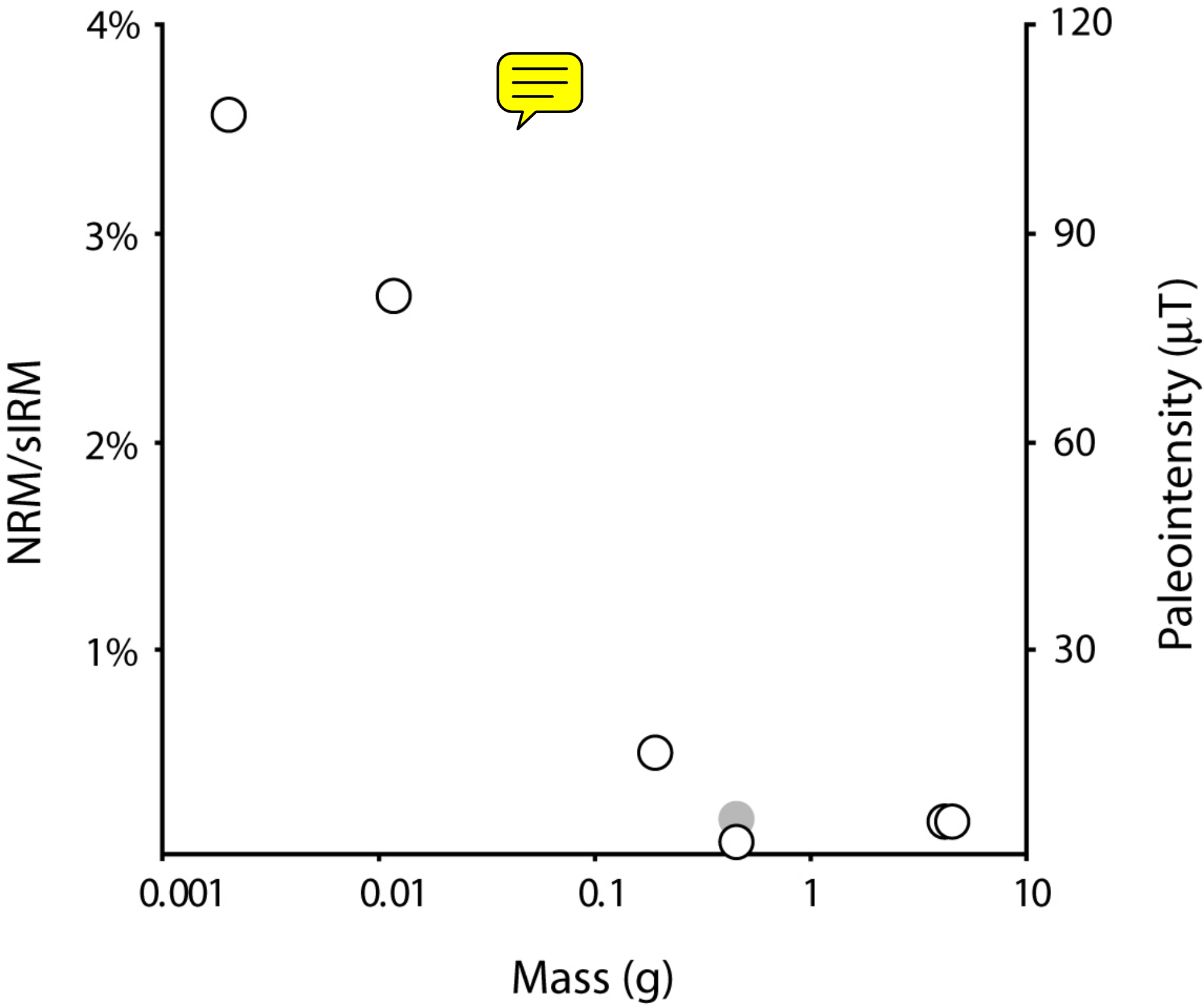
4%
3%
2%
1%
NRM/sIRM
120
90
60
30
Paleointensity (μT)
0.001
0.01
0.1
1
10
Mass (g)

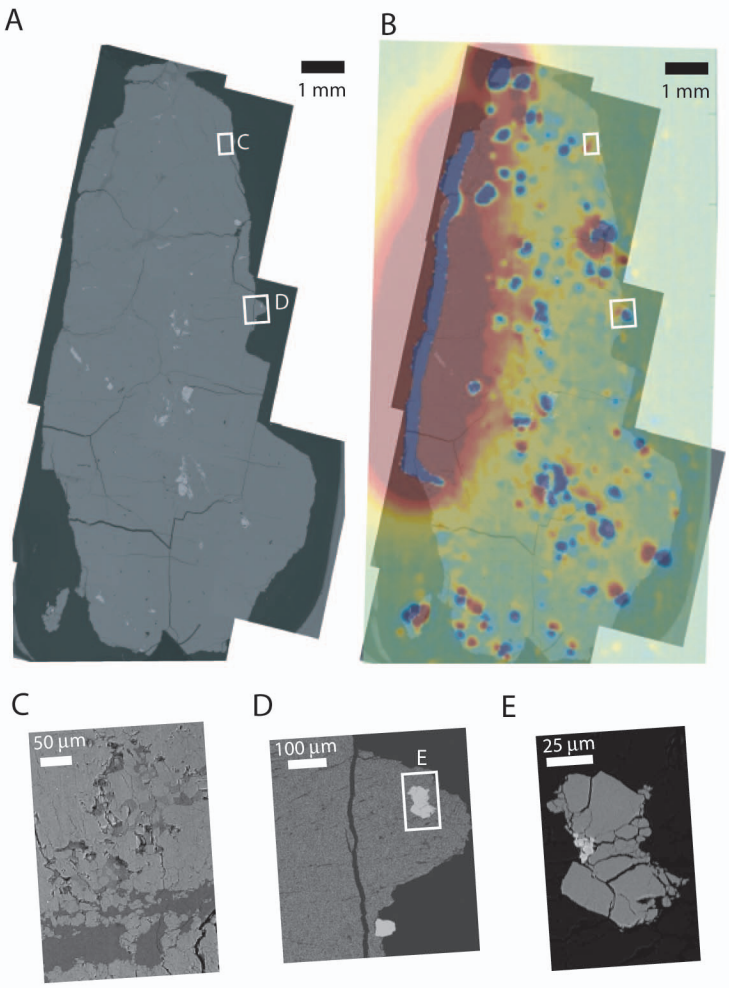
A
1 mm
C
D
B
1 mm
C
50 µm
D
100 µm
E
E
25 µm

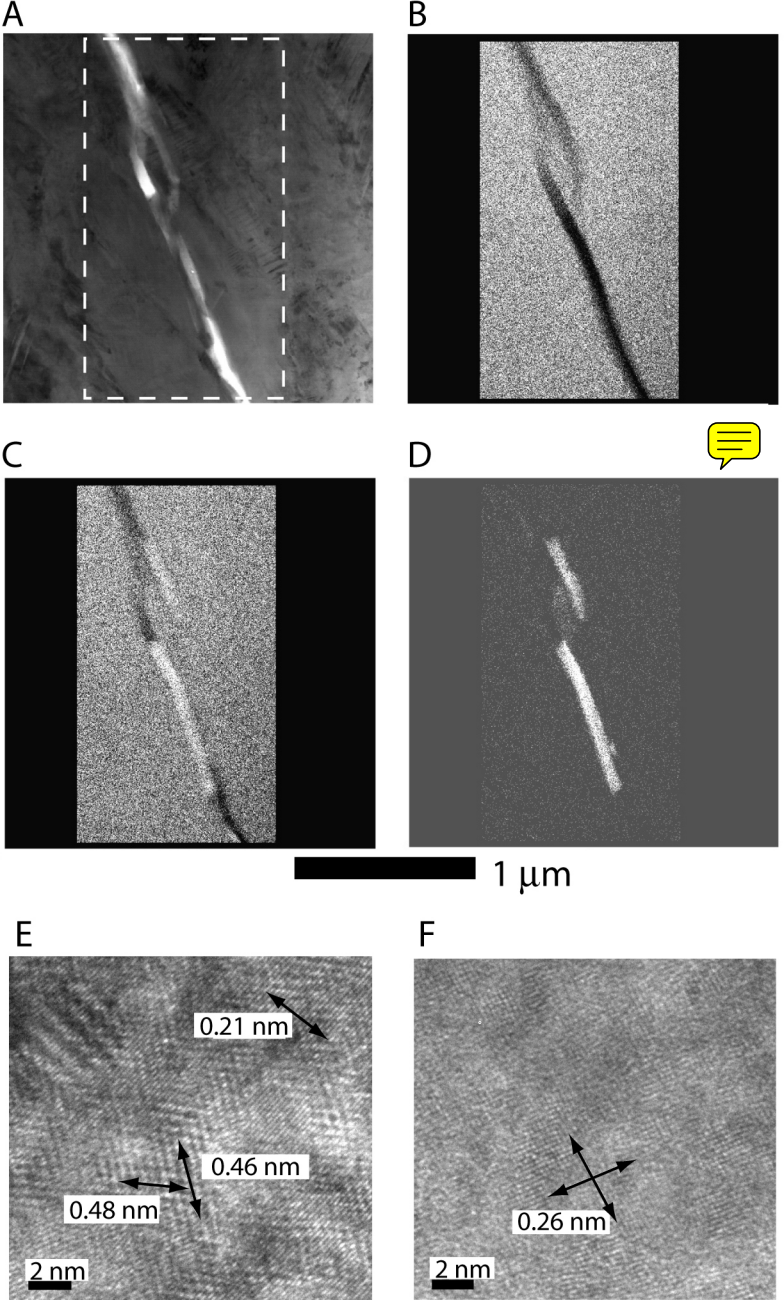
A
B
C
D
1 µm
E
0.21 nm
0.46 nm
0.48 nm
2 nm
F
0.26 nm
2 nm

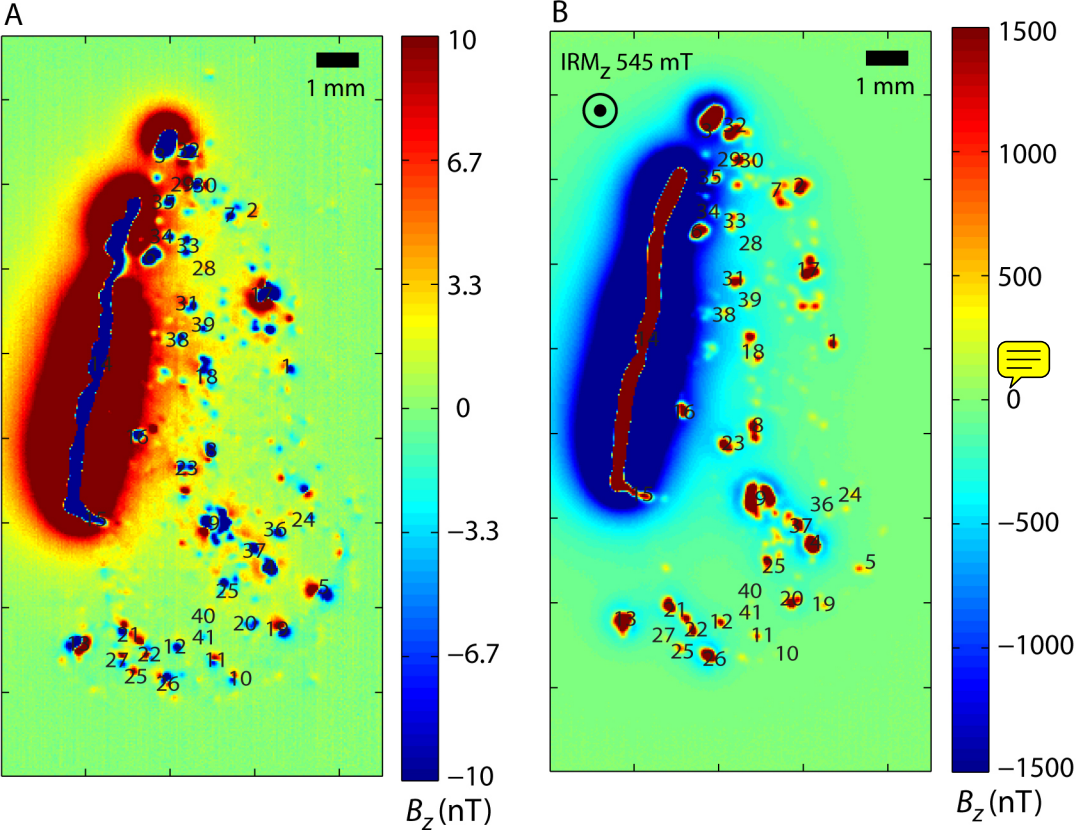
A
1 mm
10
6.7
3.3
0
−3.3
−6.7
−10
B_z (nT)
B
IRM$_z$ 545 mT
1 mm
1500
1000
500
0
−500
−1000
−1500
B_z (nT)

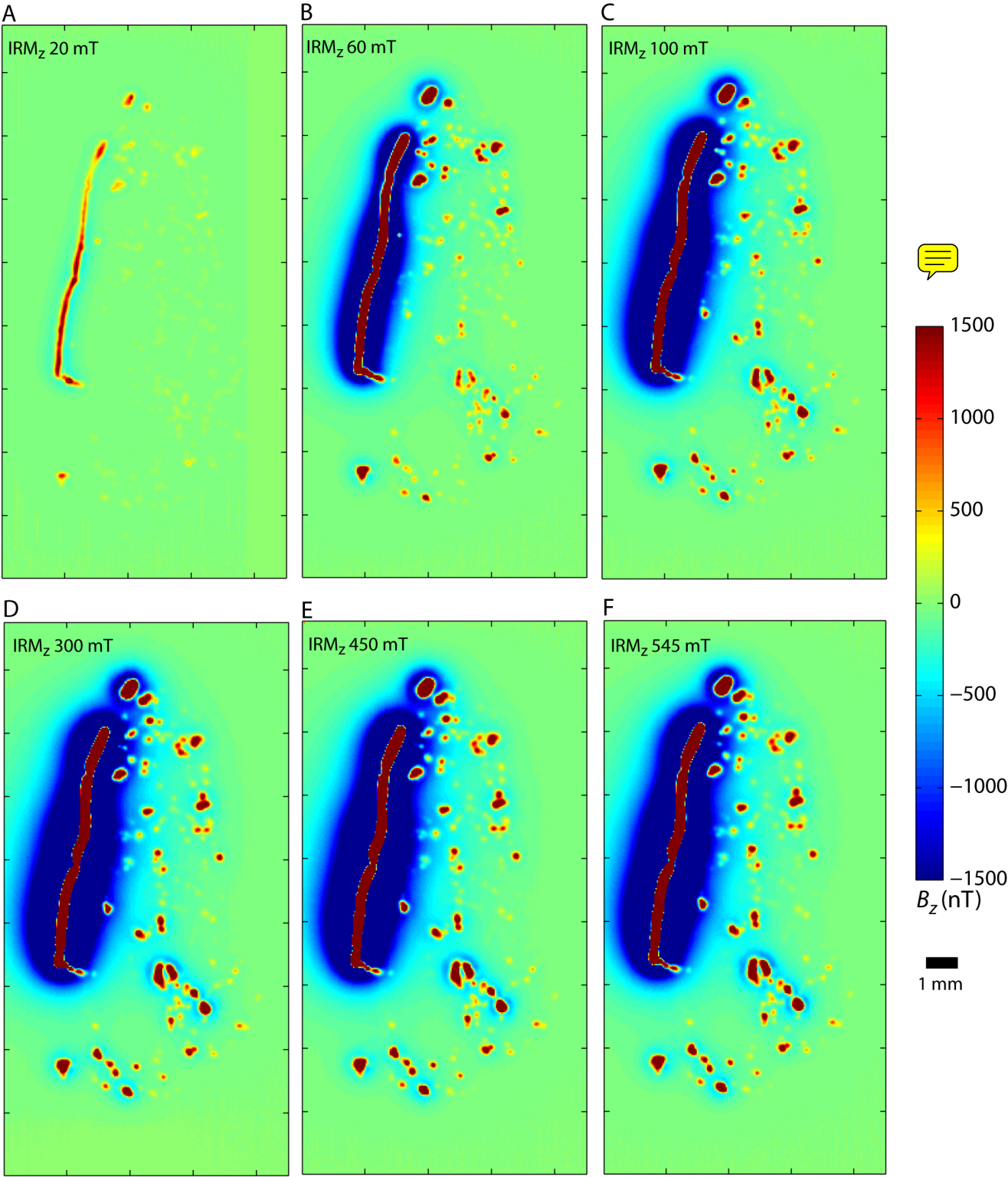
A
IRM$_Z$ 20 mT
B
IRM$_Z$ 60 mT
C
IRM$_Z$ 100 mT
D
IRM$_Z$ 300 mT
E
IRM$_Z$ 450 mT
F
IRM$_Z$ 545 mT
1500
1000
500
0
−500
−1000
−1500
B_z (nT)
1 mm

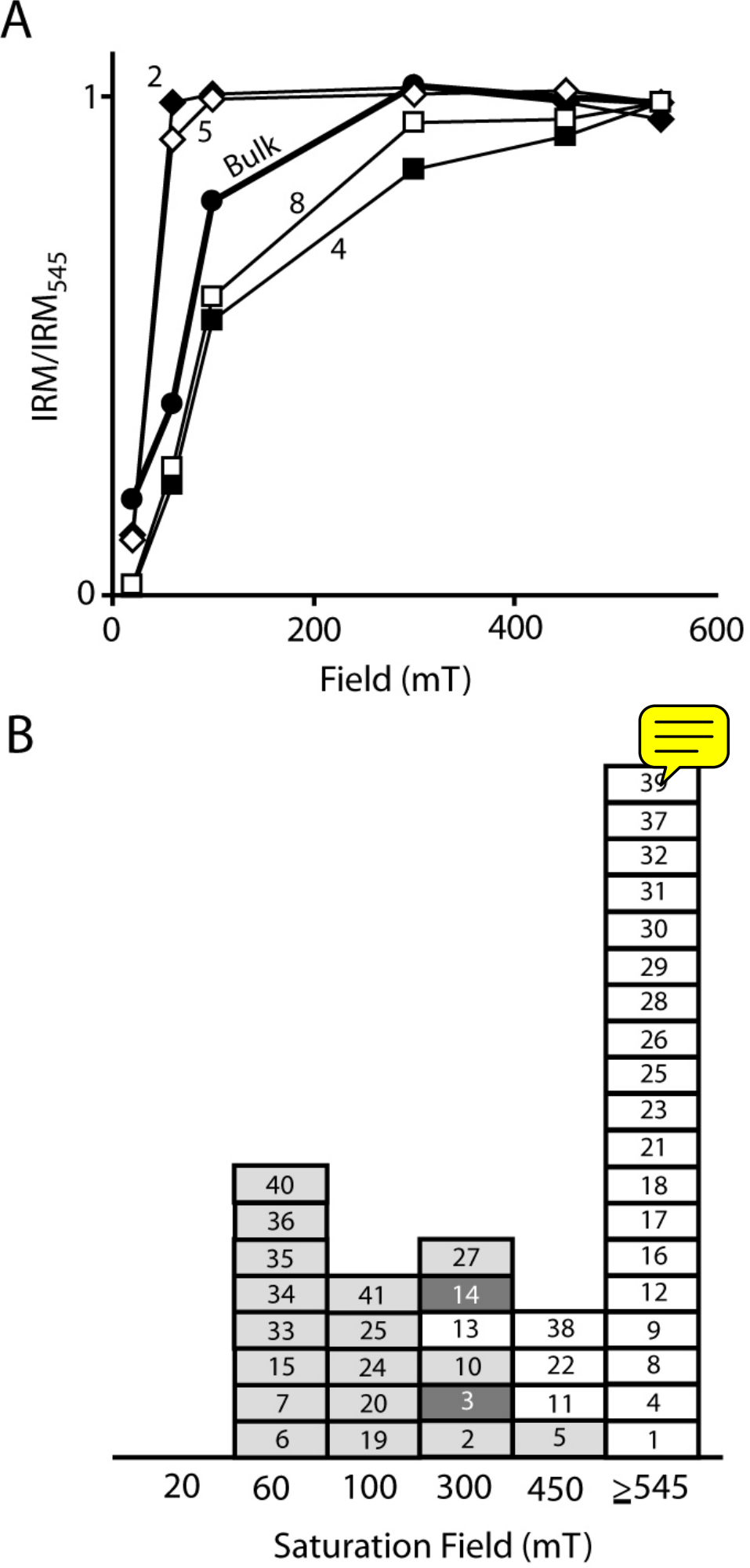
A
1
0
2
5
Bulk
8
4
IRM/IRM545
0
200
400
600
Field (mT)
B
39
37
32
31
30
29
28
26
25
23
21
18
17
16
12
9
8
4
1
40
36
35
34
33
15
7
6
41
25
24
20
19
27
14
13
10
3
2
38
22
11
5
20
60
100
300
450
≥545
Saturation Field (mT)

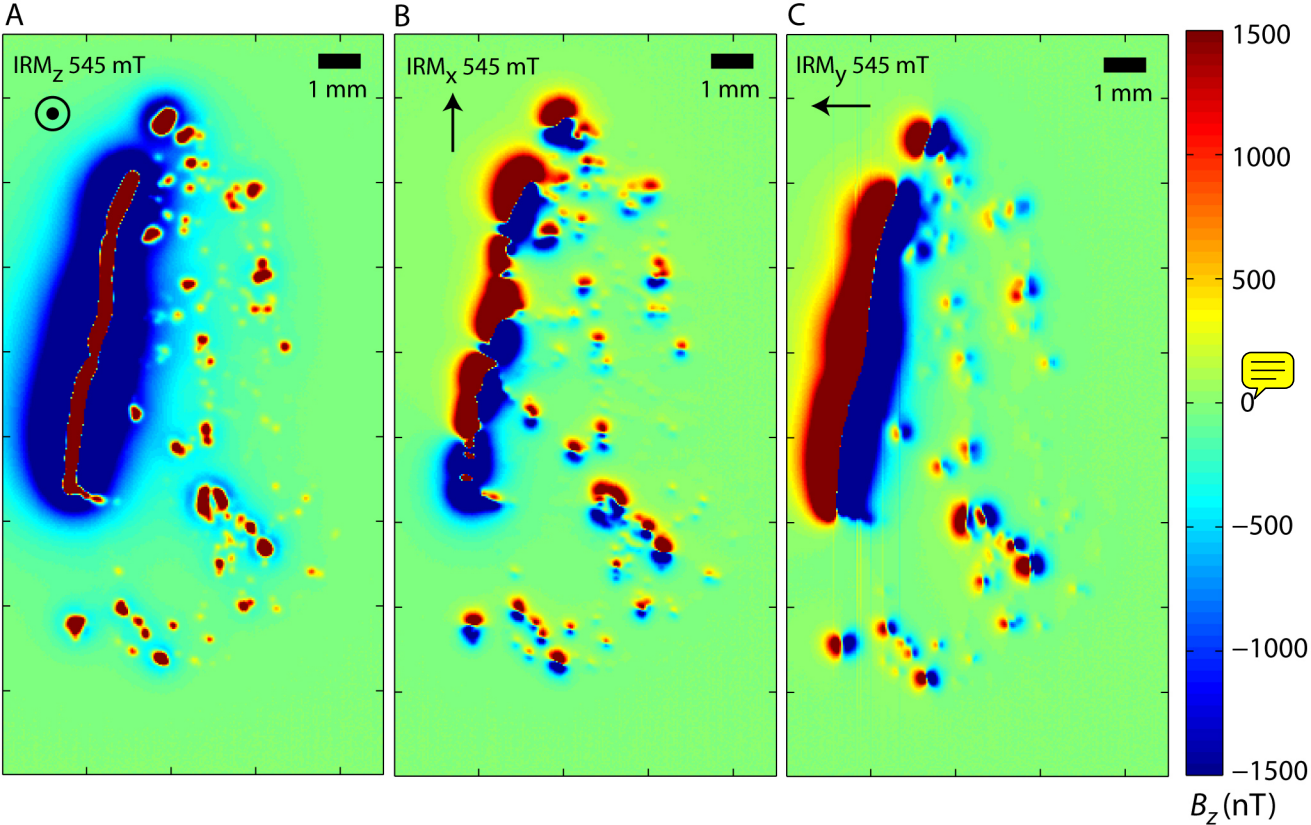
A
IRM$_z$ 545 mT
1 mm
B
IRM$_x$ 545 mT
1 mm
C
IRM$_y$ 545 mT
1 mm
1500
1000
500
0
−500
−1000
−1500
B_z (nT)

A

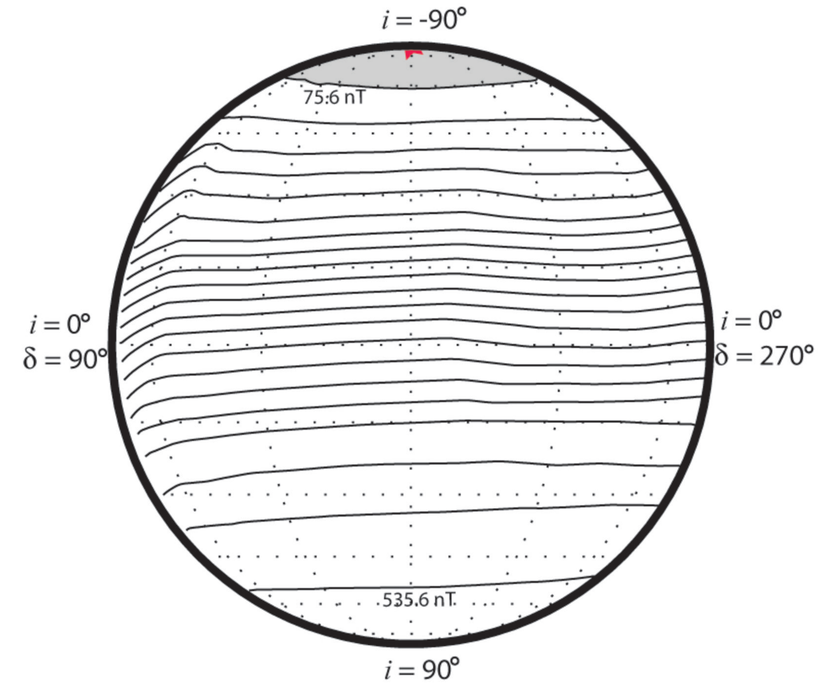

IRMz

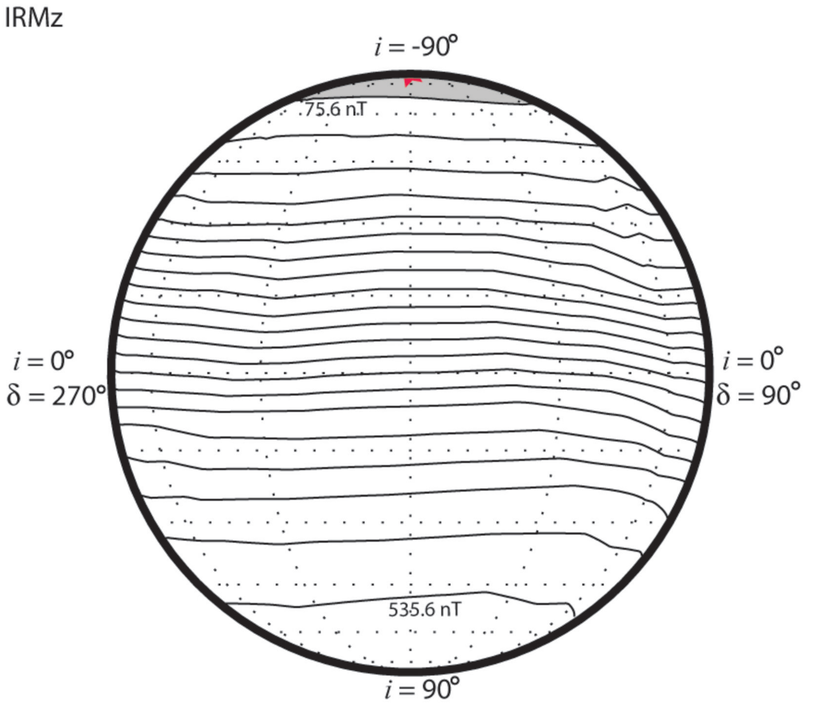

B

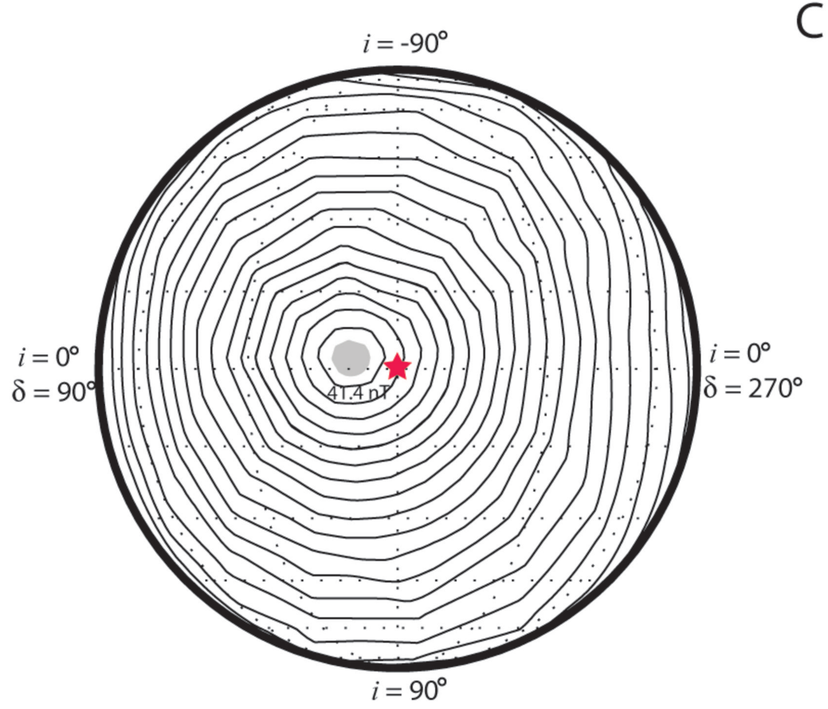

IRMx

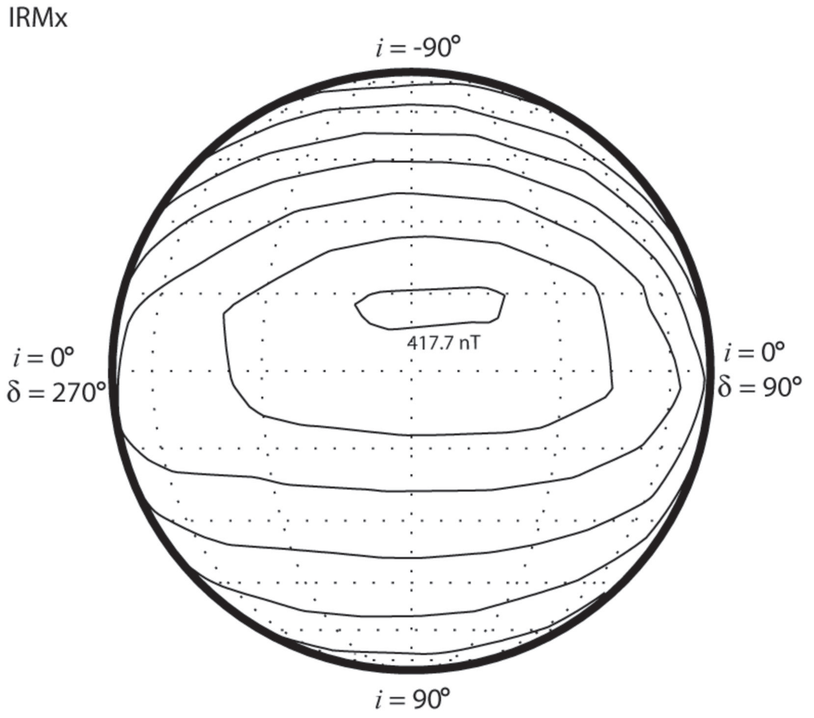

C

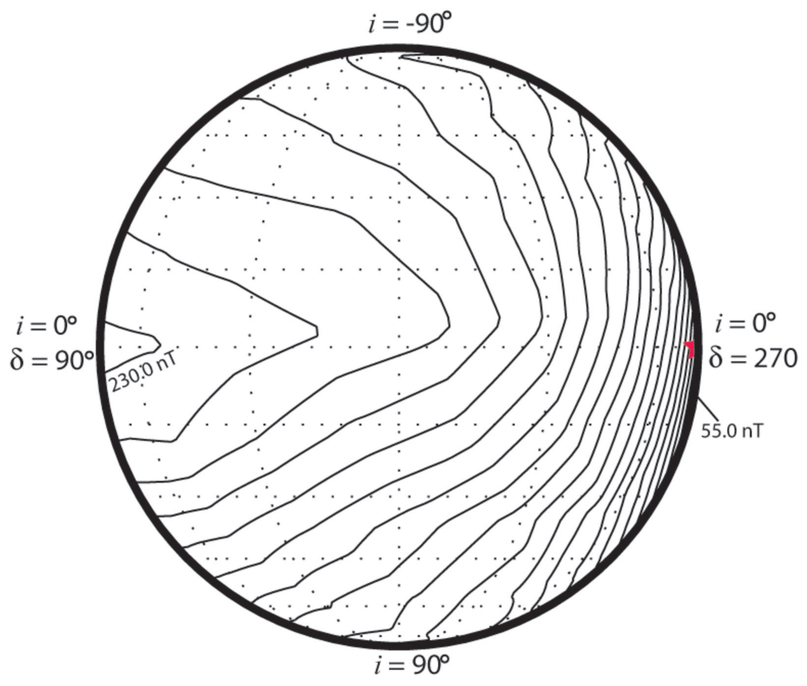

IRMy

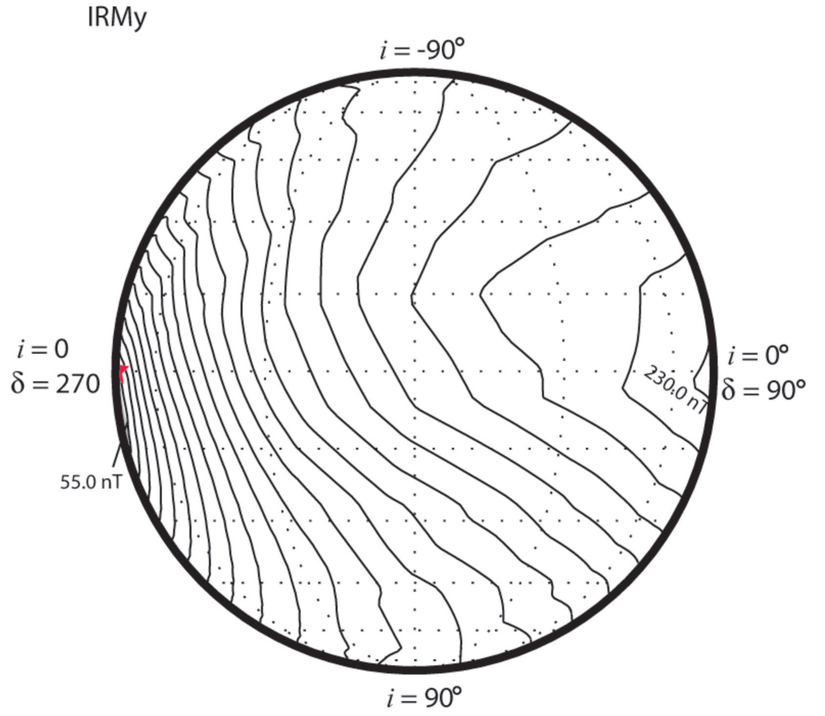

D

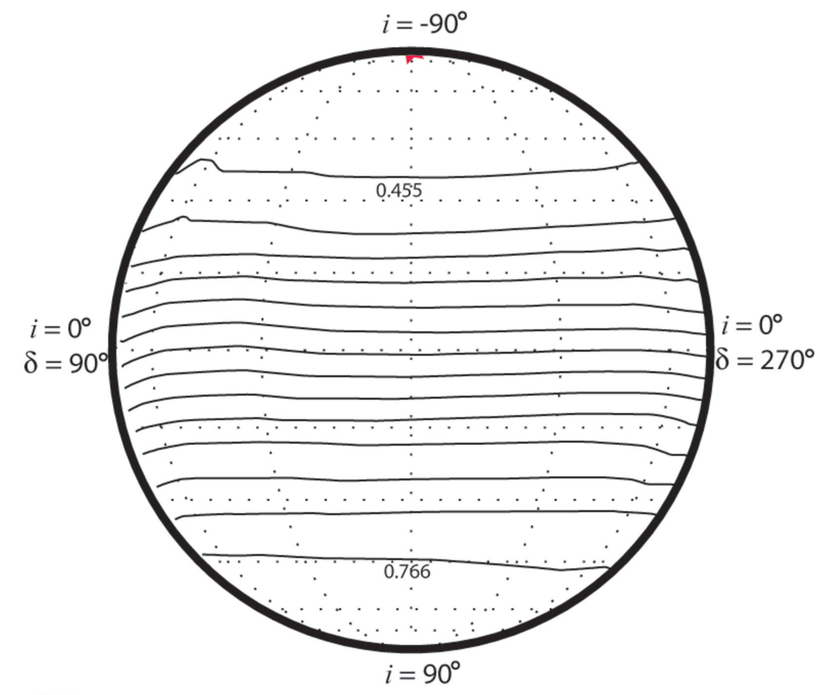

IRMz

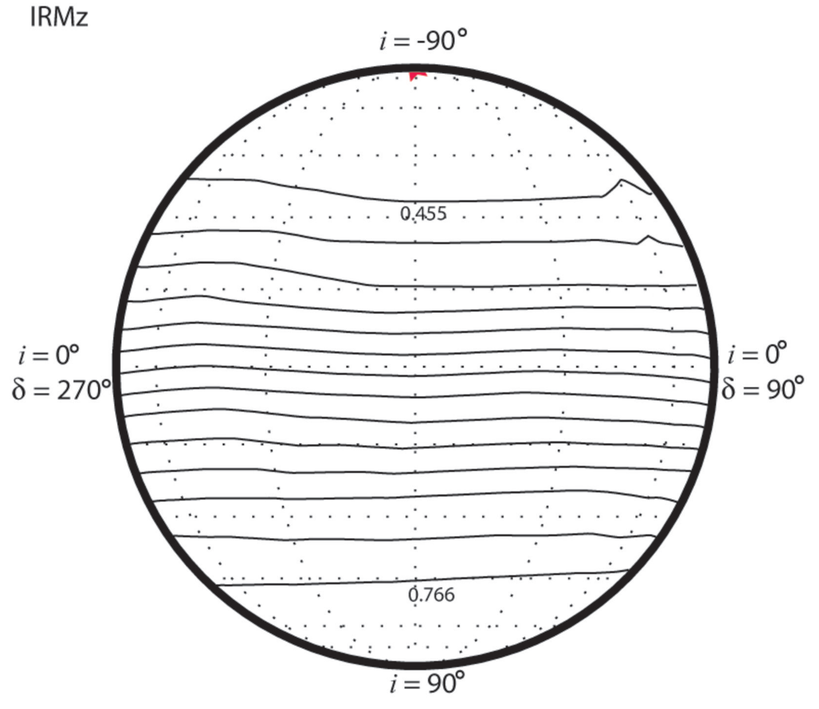

E

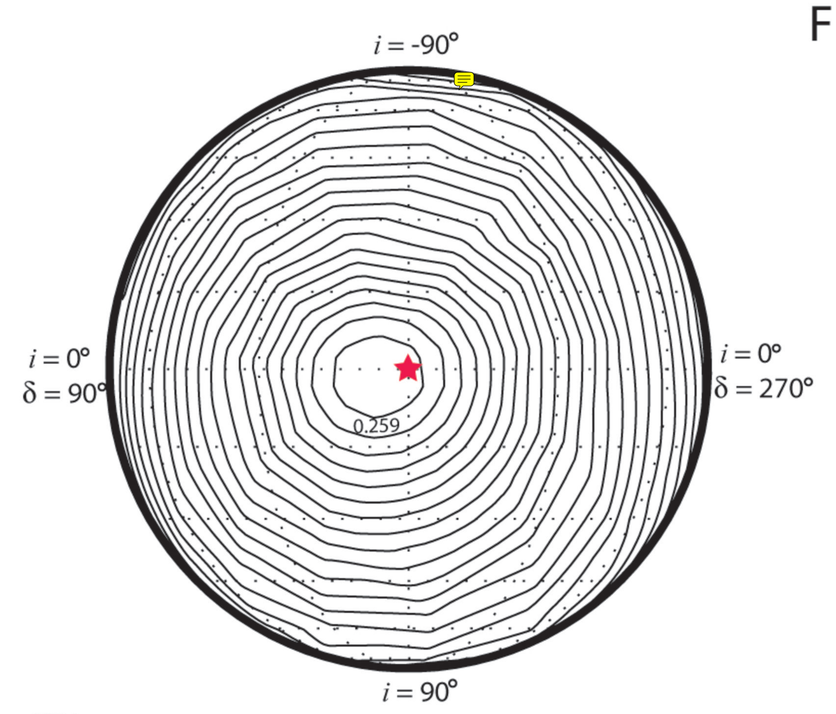

IRMx

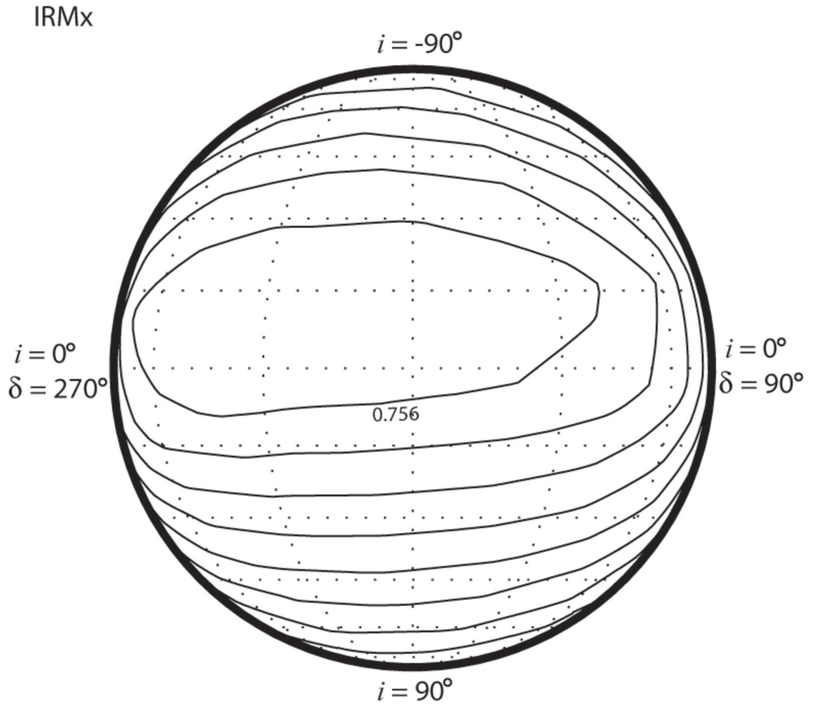

F

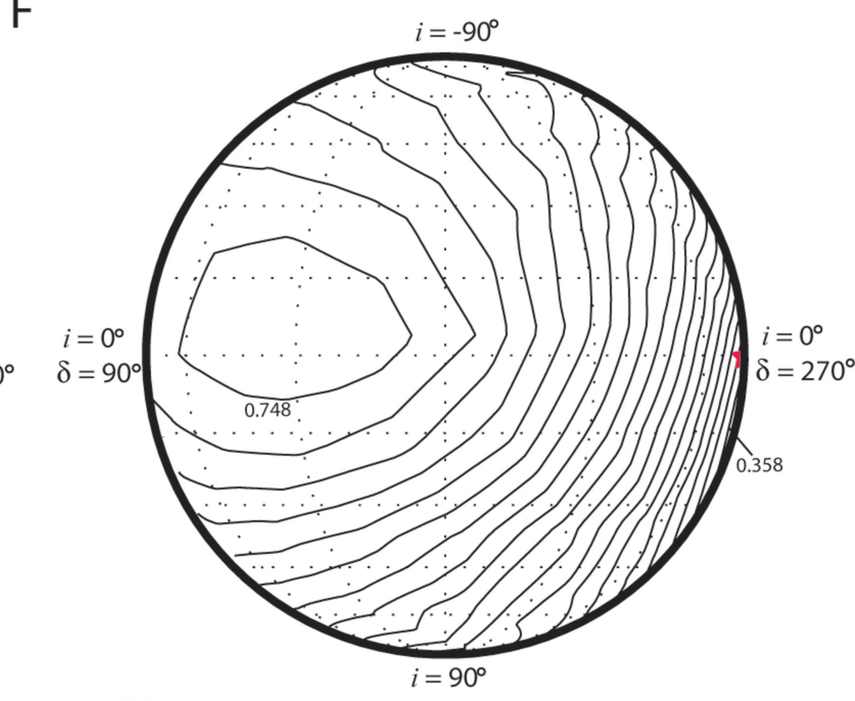

IRMy

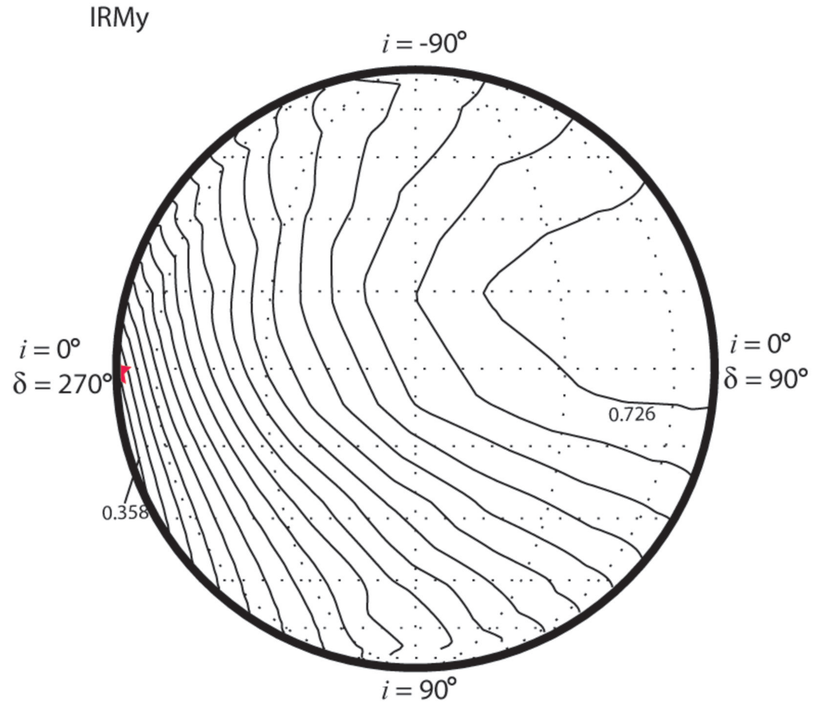

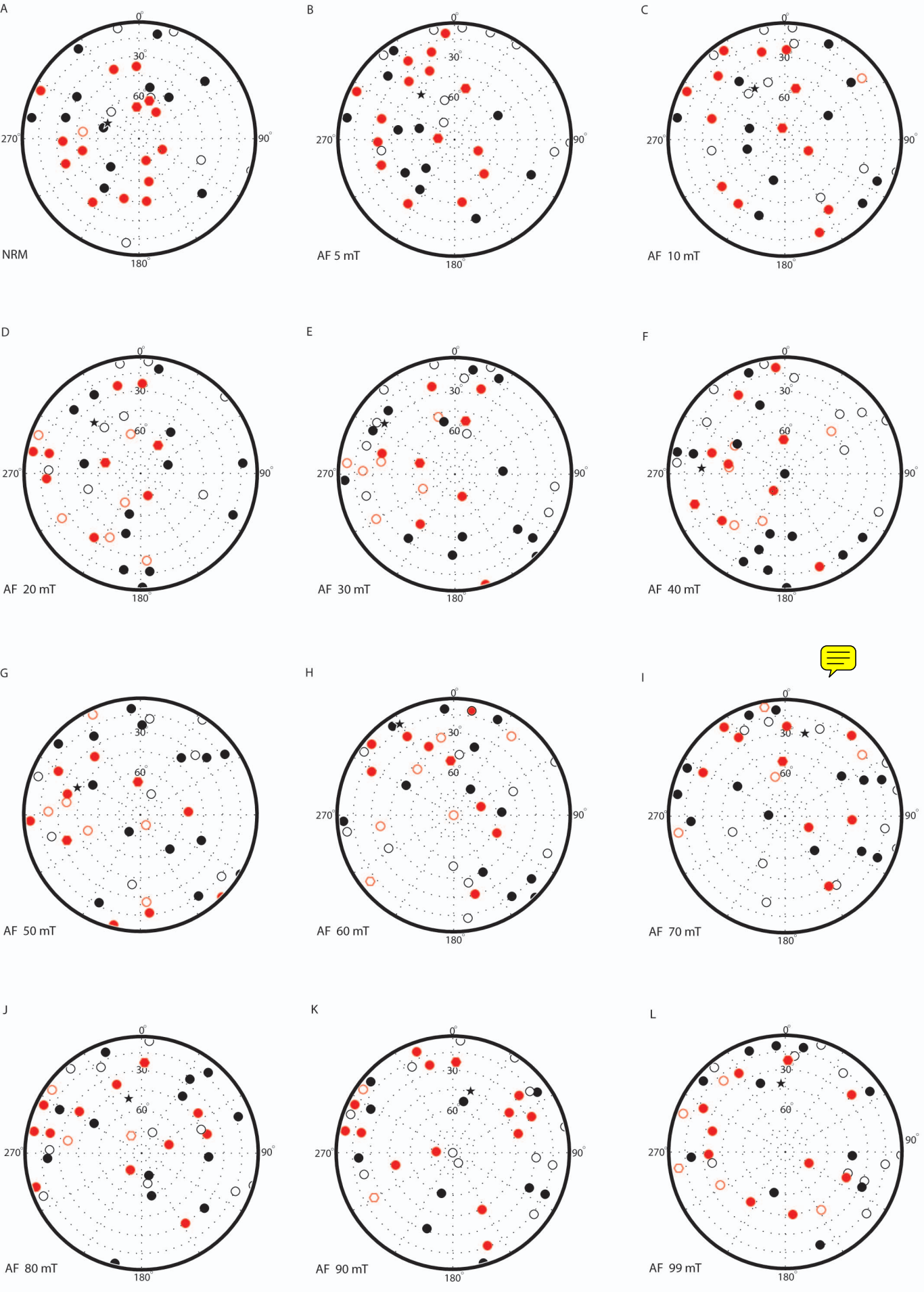
A
0°
30°
60°
270°
90°
180°
NRM
B
AF 5 mT
C
AF 10 mT
D
AF 20 mT
E
AF 30 mT
F
AF 40 mT
G
AF 50 mT
H
AF 60 mT
I
AF 70 mT
J
AF 80 mT
K
AF 90 mT
L
AF 99 mT

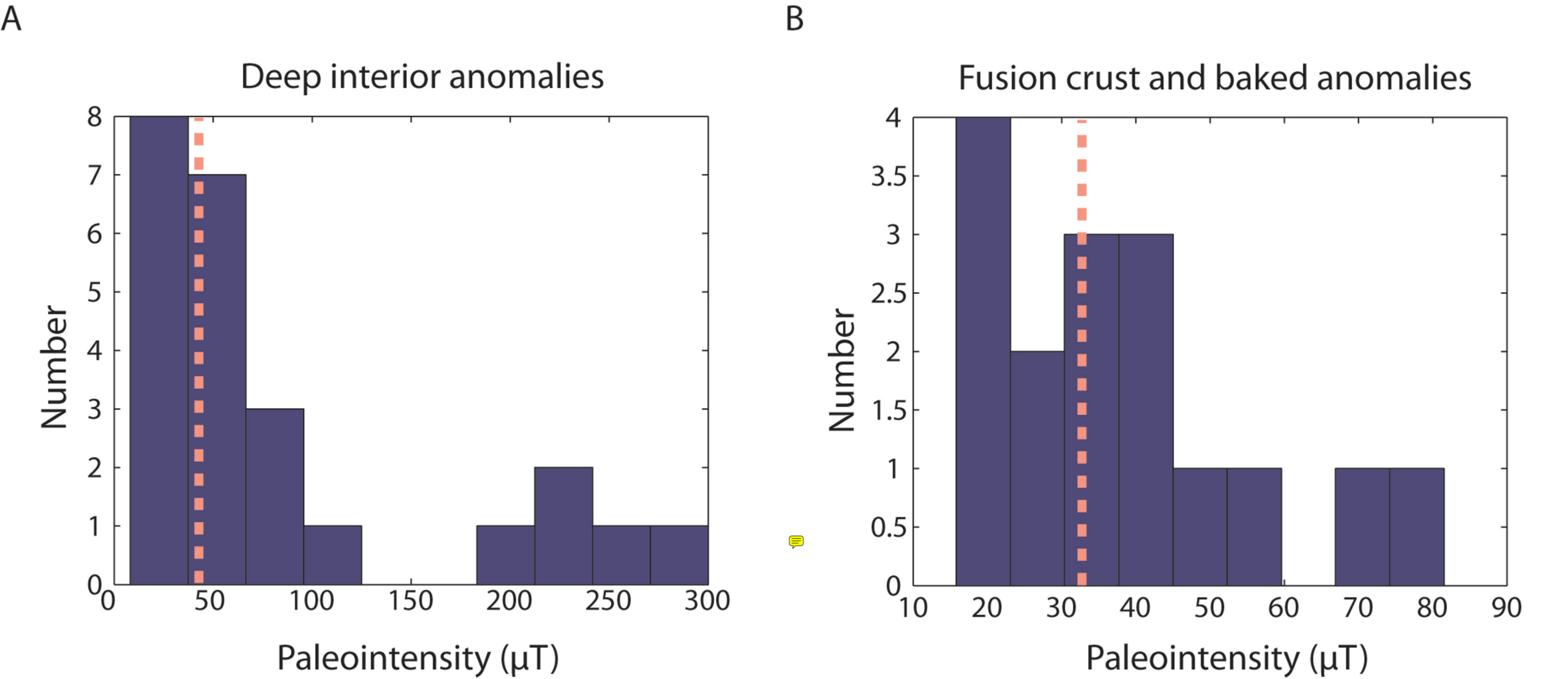
A
Deep interior anomalies
Number
Paleointensity (μT)
0
1
2
3
4
5
6
7
8
0
50
100
150
200
250
300
B
Fusion crust and baked anomalies
Number
Paleointensity (μT)
0
0.5
1
1.5
2
2.5
3
3.5
4
10
20
30
40
50
60
70
80
90